**Atmospheric
Measurement
Techniques
Discussions**

On the absolute calibration of SO$_2$ cameras

P. Lübcke[1,2], N. Bobrowski[1], S. Illing[1], C. Kern[3], J. M. Alvarez Nieves[4], L. Vogel[1], J. Zielcke[1], H. Delgado Granados[4], and U. Platt[1]

[1]Institut für Umweltphysik, Im Neuenheimer Feld 229, 69120 Heidelberg, Germany
[2]Max-Planck-Institut für Chemie, Mainz, Germany
[3]Cascades Volcano Observatory, US Geological Survey, Vancouver, WA, USA
[4]Departamento de Vulcanologica, Instituto de Geofísica, UNAM, Mexico

Correspondence to: P. Lübcke (pluebcke@iup.uni-heidelberg.de)

AMTD

5, 6183–6240, 2012

Calibration of the SO$_2$ camera

P. Lübcke et al.

Title Page

Abstract	Introduction
Conclusions	References
Tables	Figures

|◄ | ►|
| ◄ | ► |

| Back | Close |

Full Screen / Esc

Printer-friendly Version

Interactive Discussion

Abstract

Sulphur dioxide emission flux measurements are an important tool for volcanic monitoring and eruption risk assessment. The SO$_2$ camera technique remotely measures volcanic emissions by analysing the ultraviolet absorption of SO$_2$ in a narrow spectral window between 305 nm and 320 nm using solar radiation scattered in the atmosphere. The SO$_2$ absorption is selectively detected by mounting band-pass interference filters in front of a two-dimensional, UV-sensitive CCD detector. While this approach is simple and delivers valuable insights into the two-dimensional SO$_2$ distribution, absolute calibration has proven to be difficult. An accurate calibration of the SO$_2$ camera (i.e., conversion from optical density to SO$_2$ column density, CD) is crucial to obtain correct SO$_2$ CDs and flux measurements that are comparable to other measurement techniques and can be used for volcanological applications. The most common approach for calibrating SO$_2$ camera measurements is based on inserting quartz cells (cuvettes) containing known amounts of SO$_2$ into the light path. It has been found, however, that reflections from the windows of the calibration cell can considerably affect the signal measured by the camera. Another possibility for calibration relies on performing simultaneous measurements in a small area of the camera's field-of-view (FOV) by a narrow-field-of-view Differential Optical Absorption Spectroscopy (NFOV-DOAS) system. This procedure combines the very good spatial and temporal resolution of the SO$_2$ camera technique with the more accurate column densities obtainable from DOAS measurements.

This work investigates the uncertainty of results gained through the two commonly used, but quite different calibration methods (DOAS and calibration cells). Measurements with three different instruments, an SO$_2$ camera, a NFOV-DOAS system and an Imaging DOAS (IDOAS), are presented. We compare the calibration-cell approach with the calibration from the NFOV-DOAS system. The respective results are compared with measurements from an IDOAS to verify the calibration curve over the spatial extend of the image.

Our results show that calibration cells can lead to an overestimation of the SO_2 CD by up to 60 % compared with CDs from the DOAS measurements. Besides these errors of calibration, radiative transfer effects (e.g. light dilution, multiple scattering) can significantly influence the results of both instrument types. These effects can lead to an even more significant overestimation or, depending on the measurement conditions, an underestimation of the true CD. Previous investigations found that possible errors can be more than an order of magnitude. However, the spectral information from the DOAS measurements allows to correct for these radiative transfer effects. The measurement presented in this work were taken at Popocatépetl, Mexico, between 1 March 2011 and 4 March 2011. Average SO_2 emission rates between 4.00 kg s^{-1} and 14.34 kg s^{-1} were observed.

1 Introduction

Today SO_2 fluxes are starting to be routinely monitored at a considerable number of volcanoes for volcanic risk assessment – largely by the Network for Observation of Volcanic and Atmospheric Change (NOVAC, Galle et al., 2010). The chemical lifetime of SO_2 in the atmosphere (typically several days) is long compared to plume ages (minutes to hours) typically observed by ground-based remote sensing measurements (e.g., Oppenheimer et al., 1998; von Glasow et al., 2009). Moreover, its low background concentration in the atmosphere makes volcanic SO_2 easy to identify by remote sensing techniques. Since the correlation spectrometer (COSPEC) was first used in the 1970s (e.g., Moffat and Millan, 1971; Stoiber et al., 1983) the remote sensing of volcanic gases has evolved and Differential Optical Absorption Spectroscopy (DOAS, Platt and Stutz, 2008) currently is, together with the continuing use of COSPEC, the most frequently applied technique. Apart from the advantage of lower cost of instruments when compared to the COSPEC, DOAS can be used to identify various trace gases simultaneously by their distinguishable differential absorption features. SO_2 is analysed in this work but, NO_2, BrO or O_3 can, for instance, be measured as well.

DOAS is applied at volcanoes in various implementations. One commonly used method involves scanning DOAS systems that measure in a narrow FOV and perform scans through a cross-section of the volcanic plume by moving the telescope and recording spectra at different elevation angles. This approach is used by the NOVAC-network for instance. A drawback of scanning DOAS systems is that it may take several minutes to complete a scan through the cross section of a volcanic plume. Other instruments use UV spectrometers with a wide FOV telescope (i.e., two spectrometers equipped with optical systems that capture light from an entire plume cross section at once) to obtain flux measurements with a higher temporal resolution (McGonigle et al., 2009; Boichu et al., 2010). While the wide FOV method has a time resolution of the order of 1 Hz, similar to the SO$_2$ camera, it is limited in spatial information. Furthermore, an additional error may be introduced due to the summation over a possibly broad range of intensities in the FOV.

With the scanning DOAS, the wide FOV instrument and the SO$_2$ camera the wind speed can be calculated by comparing time series of SO$_2$ column densities at two different distances from the volcanic vent. The time the plume needs to travel between the two distances is found by using cross-correlation between time series of the respective measurements (e.g., McGongile et al., 2005; Johansson et al., 2009; Galle et al., 2010; Boichu et al., 2010).

The Imaging DOAS (IDOAS) is an instrument that allows the spectroscopic measurement of two-dimensional trace gas distributions. Typical IDOAS instruments such as the one used during our measurements, take approximately 20 minutes to acquire a two-dimensional image of the trace gas distribution. During this time it produces an image that has a horizontal field-of-view comparable to our SO$_2$ camera (22.4°).

The DOAS technique has important advantages: besides the ability to resolve different species in a single measurement it offers the possibility to treat radiative transfer issues (like multiple scattering inside the volcanic plume or the light dilution effect) through the availability of spectral information (Kern et al., 2010a). Nevertheless all

Title Page

Abstract | Introduction

Conclusions | References

Tables | Figures

|◄ | ►|

◄ | ►

Back | Close

Full Screen / Esc

Printer-friendly Version

Interactive Discussion

DOAS measurement geometries require compromising on either spatial or time resolution.

In contrast to standard DOAS measurements, the SO$_2$ camera can measure two-dimensional SO$_2$ CD distributions with a high spatial resolution and a high frequency of the order of 1 Hz with, however, extremely reduced spectral information. The measurement principle employs one or two interference filters and a UV-sensitive CCD. One filter (Filter A) measures the optical density of SO$_2$, a second filter (Filter B) is used to correct for aerosol scattering and radiative transfer effects (Mori and Burton, 2006; Dalton et al., 2009; Kantzas et al., 2010; Kern et al., 2010a).

Because aerosol scattering on particles with diameters of the order of the radiation wavelength actually does exhibit a slight wavelength dependency the second filter can not completely remove the influence of aerosol and plume condensation on the measurement results.

While SO$_2$ cameras are certainly limited by the fact that only one trace gas can be measured and that radiative transfer effects can potentially lead to an inaccurate calibration, the SO$_2$ camera can nevertheless be an important tool for measuring SO$_2$ fluxes under certain conditions; in particular for measuring the total SO$_2$ emitted during an event (Mori and Burton, 2009) or when the wind speed is spatially variable. The high time resolution of the SO$_2$ camera allows the observation of dynamic effects in the volcanic plume and therefore can be used to obtain SO$_2$ emission rates at time resolutions on the order of a second. In fact, it was recently shown that optical flow models can be applied to derive 2-dimensional plume velocity fields (see Kern et al., 2012a). Further advantages of high time resolution SO$_2$ emission flux data lie in the synergetic use of several geophysical methods which in combination will allow better interpretation of the volcanic activity signals (e.g., Dalton et al., 2010; Nadeau et al., 2011). For a better integration of various data sets, it is important that they have a comparable time resolution. In particular, the SO$_2$ camera's time resolution of 1 Hz is ideal for the integration of seismic and gas emission data.

The SO_2 camera measures the optical density of SO_2. In the case of a two filter SO_2 camera it is called the apparent absorbance (AA). This is the differential optical density τ determined from the difference between the optical densities of the two filters (see e.g., Mori and Burton, 2006). For the calculation of SO_2 fluxes the first crucial step is to calibrate the SO_2 camera. A procedure has to be given to convert AA values to SO_2 CDs, i.e., the number density of SO_2 integrated over the light path (e.g. Kern et al., 2010b).

Errors made during the conversion directly influence the obtained SO_2 flux and therefore propagate into all quantities derived from the flux, such as the total SO_2 emitted during an event or the mass of magma involved in the degassing processes. Misleading conclusions may easily be drawn from such data sets and can lead to incorrect conclusions about the volcanic system.

The camera calibration is mostly performed with calibration cells (Bluth et al., 2007; Dalton et al., 2009; Kantzas et al., 2010), but can also be performed by taking simultaneous measurements with a DOAS system.

In this paper we present results from a measurement campaign at Popocatépetl volcano (Mexico) in March 2011. We compare calibration curves obtained from DOAS measurements with those obtained from the calibration cells and determine the magnitude of error for the calibration-cell method that we observed during our measurements.

2 The measurement principle of the SO_2 camera

When scattered solar radiation passes through a volcanic plume, it is influenced by gases, ash and aerosol in the plume. The SO_2 camera measures the differential optical density of SO_2 by applying one or two band-pass filters (Mori and Burton, 2006; Bluth et al., 2007). Filter A transmits radiation in a region where SO_2 absorption is prominent and still sufficient solar radiation intensity is available to allow reasonable exposure times. This is the case for the wavelength region between 305 nm and 320 nm. Therefore, the measured intensity $I_{A,M}$ is influenced by SO_2 absorption, but also by aerosols,

Full Screen / Esc

Printer-friendly Version

Interactive Discussion

ash and plume condensation. The optical density τ_A for Filter A can be written as:

$$\tau_A = -\ln \frac{I_{A,M}}{I_{A,0}} \qquad (1)$$

with incident spectral radiation intensity $I_{A,0}$ and radiation intensity $I_{A,M}$ after passing through the volcanic plume.

5   A first order correction can be performed with a second filter that transmits radiation in a region where SO_2 absorption is negligible, but the influence of the other effects is comparable (325 to 335 nm). This correction is based on the assumption that these effects are spectrally flat between 305 nm and 335 nm.

The optical density τ_B for Filter B is not influenced by SO_2 absorption:

10    $$\tau_B = -\ln \frac{I_{B,M}}{I_{B,0}} \qquad (2)$$

The AA is the difference between the optical densities for Filter A and Filter B:

$$\tau = AA = \tau_A - \tau_B = -\ln \frac{I_{A,M}}{I_{A,0}} + \ln \frac{I_{B,M}}{I_{B,0}}$$

$$= \ln \frac{\frac{I_{B,M}}{I_{B,0}}}{\frac{I_{A,M}}{I_{A,0}}} = \ln \frac{I_{B,M}}{I_{A,M}} \cdot \frac{I_{A,0}}{I_{B,0}} \qquad (3)$$

Since the AA cannot directly be used to calculate the SO_2 flux, a calibration has to be performed to convert AA values to SO_2 CDs.

3   Instruments applied during the measurements at Popocatépetl, Mexico

An SO_2 camera system with an integrated NFOV-DOAS system was designed and build in our laboratory at the University of Heidelberg. Field measurements were conducted at Popocatépetl, Mexico, together with an IDOAS instrument, which was also

custom-built in our laboratory. All three instruments (SO_2 camera, NFOV-DOAS and IDOAS) will be briefly described in this section. More detailed information about the IDOAS can be found in Louban et al. (2009).

3.1 Design and instrumental set-up of the SO_2 camera

The central element of our SO_2 camera is an Apogee Instruments Alta U6 CCD array which serves as a detector. The array consists of 1024×1024 pixels with a pixel size of $24 \times 24\,\mu m$ resulting in a large detector area of $24.58 \times 24.58\,mm$. Short exposure times (approximately 0.2–0.4 s) can therefore be achieved despite the fact that the detector quantum efficiency Q and the scattered radiation intensity are low in the UV regions used in the measurements. The optical set-up (see Fig. 2) consisted of a single 31.5 mm diameter plano convex fused silica lens with a focal length of $f = 60\,mm$ and two band-pass interference filters mounted in a filter wheel between the lens and the detector. This set-up was chosen to reduce influences from a variable filter illumination angle (see Kern et al., 2010b, for more detailed information about this effect). An iris aperture was installed directly in front of the lens. Aperture settings were only adjusted at the beginning of the measurement campaign, as changes in the aperture influence the calibration (see Sect. 4.1).

While conducting the measurements presented here, an aperture of roughly $f/8$ was used. Two interference filters from Eureca Messtechnik with a central transmittance wavelength of 315 nm (Filter A , FWHM 10 nm), and 330 nm (Filter B, FWHM 10 nm), were used for the measurements.

The filters are installed in a custom-made filter wheel that consists of an aluminium mount, which holds the two filters, and a standard servo unit (as, e.g., used in model air planes), which is operated by a Phidgets[©] USB servo controller (PhidgetAdvancedServo 8-Motor). The Phidget[©] controller also controls two further servo motors. These servo motors can each insert one of two calibration cells containing known SO_2 concentrations in front of the aperture, each covering the entire FOV of

Calibration of the SO_2 camera

P. Lübcke et al.

Title Page

Abstract	Introduction
Conclusions	References
Tables	Figures

◄◄	►►
◄	►
Back	Close

Full Screen / Esc

Printer-friendly Version

Interactive Discussion

the camera. The calibration cells were filled with SO$_2$ concentrations corresponding to column densities of 3.5×10^{17} molec cm^{-2} and 1.8×10^{18} molec cm^{-2}, respectively. The calibration cells can be moved in the light path separately or at the same time, thus giving three measurement points for calibration. More calibration cells would improve the quality of the calibration curve but also drastically increase the mechanical complexity of the camera.

3.2 The Narrow Field of View-DOAS

For calibration purposes a Narrow Field of View DOAS (NFOV-DOAS) system was installed inside the camera housing. It measures the SO$_2$ CD at the approximate centre of the camera image (see Fig. 1 and Kern et al., 2010b). The DOAS system consists of an Ocean Optics USB2000+ spectrometer, a 400 µm fibre, a Hoya U330 filter to reduce stray light, and a telescope with a quartz lens with a focal length of $f = 30$ mm and a diameter of 18.5 mm. The telescope of the DOAS system is mechanically attached to the camera optics to minimize changes in the FOV relative to the camera images. The spectrometer temperature was stabilized to 15 °C for all measurements presented. This was done with a peltier element controlled by an Arduino board (Arduino Uno manufactured by SmartProjects) running a PID control software, and an Analog Devices ADT7410 temperature sensor. The spatial resolution, FOV and the exposure times used during our measurements are summarized in Table 1.

3.3 The Imaging DOAS instrument

The Imaging DOAS (IDOAS) is an instrument that uses a two-dimensional CCD as a detector in an imaging spectrometer to measure two-dimensional trace gas CDs. During our measurements, the horizontal direction of the CCD was used to resolve spectral information, while the vertical direction was used to capture one spatial dimension. The second spatial dimension (horizontal direction) is obtained by applying the push-broom method, realized by rotating a mirror to scan along the second spatial

Full Screen / Esc

Printer-friendly Version

Interactive Discussion

dimension (Lohberger et al., 2004; Bobrowski et al., 2006; Louban et al., 2009). The IDOAS instrument uses a quartz lens with $f = 30\,mm$ ($d = 20\,mm$) to image the incident radiation onto the entrance slit of the spectrograph (Jobin Yvon UFS-200, $f = 21\,cm$, $f/\# = 3.2$, grating: 1200 lines mm^{-1}), an Andor DV-420-OE (1024 pixel columns by 255 pixel rows) serves as a detector. Measurements were conducted simultaneous to the SO$_2$ camera observations on 4 March 2011 to compare the NFOV-DOAS calibration with a second instrument and to verify the calibration over the spatial extend of the image instead of only the small region captured by the NFOV-DOAS. Information about the spatial resolution, FOV and settings are shown in Table 1.

4 Calibrating the SO$_2$ camera

A calibration has to be performed to convert AA values to SO$_2$ column densities. The camera calibration depends on the incoming solar radiation (i.e., the solar zenith angle, solar azimuth angle, most importantly changes in strength of stratospheric O$_3$ absorptions), therefore the calibration typically has to be performed several times per day. Kantzas et al. (2010) found the calibration to be constant on the order of an hour during daytime, and more variable near sunrise or sunset. The camera calibration can be performed in several ways:

1. Calibrating with SO$_2$ filled calibration cells, which are placed in front of the camera. This is probably the most commonly used method today (e.g., Mori and Burton, 2006; Dalton et al., 2009; Kantzas et al., 2010).

2. DOAS measurements are used for first-order corrections of in-plume ash and aerosols (Holland et al., 2011) but can also solely be used to calibrate the camera. A DOAS instrument that measures in a small area of the camera image (see Fig. 1) produces SO$_2$ CD/AA pairs from which a calibration curve can be derived. A measurement set-up of an SO$_2$ camera with a co-aligned DOAS system can

Title Page

Abstract | Introduction

Conclusions | References

Tables | Figures

◄ | ►

◄ | ►

Back | Close

Full Screen / Esc

combine the strengths of both techniques and result in accurate SO$_2$ flux measurements with a high spatial and temporal resolution.

3. Simultaneous IDOAS measurements (e.g., Louban et al., 2009) can be used for calibration as well. However, the instrumental set-up is complicated and measurements are slow.

The calibration with quartz cells will be referred to as cell calibration (see Sect. 4.1), calibration from DOAS measurements will be referred to as DOAS calibration (see Sect. 4.2).

To calibrate correctly, we have to take reflections on the walls of the calibration cell into account, these will be discussed in Sect. 4.4. The influence of aerosols on the calibration curve will be discussed in Sect. 4.5.

4.1 The calibration cell method

When taking images through a calibration cell with known SO$_2$ CD, that covers the camera's entire FOV, the cell and background images through each filter can be used to derive an AA value (see Eq. 3) for each image pixel. A calibration curve can be obtained from AA/CD pairs derived from several measurements with calibration cells containing different SO$_2$ concentrations.

In practice, camera calibration with cells can be performed in several ways: the most simple approach is to manually place calibration cells in front of the camera. When calibration cells are placed in front of the camera (i.e., on the object-side of the camera lens) covering the complete field of view, a calibration curve for each pixel of the image can be obtained. However, automated insertion of the cells is also possible, as in our case (see Sect. 3.1), but increases the complexity of the instrument.

Another method, mentioned in Dalton et al. (2009), is using several calibration cells (with different column densities) that are attached to a mount and are distributed within the FOV of the camera, with each cell covering a (small) area within the FOV. While several calibration cells in a single image reduce the time needed for calibration image

acquisition, there are disadvantages. If the camera's response to a given SO_2 column varies at different positions within the image and the calibration cells are not placed in the same position for all measurements, the calibration curve will become unreliable. The variation of response to a given SO_2 CD is caused by variations of the transmis-
5   sion curves of the interference filters with changing illumination angle (see Kern et al., 2010b, and Sect. 4.3).

Moreover for both methods mentioned above, rays entering the camera through the calibration cell traverse the cell at different angles and thus travel different distances through the cell. This leads to somewhat different SO_2 column densities in different
10   parts of the image, which can be corrected by applying geometrical considerations.

4.2 The DOAS calibration method

As mentioned above a DOAS system that has a FOV matching a small area of the camera image can be used for calibration (Kern et al., 2010b). If the plume passes the FOV of the telescope, the spectrometer measures several SO_2 CD values while
15   the camera measures the corresponding AA values. From these values, a calibration curve from data measured directly in the volcanic plume can be obtained. With this method changes of the calibration that result from changing incoming solar radiation or from condensation and aerosols in the volcanic plume can be identified. The spectro- scopic data from the DOAS instrument can also be used for more sophisticated radia-
20   tive transfer corrections (Kern et al., 2010a). Radiative transfer effects, such as the light dilution effect (radiation scattered into the light path between the volcanic plume and instrument) or multiple scattering inside the volcanic plume, can lead to large errors. Underestimation or overestimation of the true CD are both possible.

For an exact calibration two further conditions have to be fulfilled

25   1. The DOAS calibration should cover the entire range of appearing SO_2 column densities. Care has to be taken, that over time the DOAS telescope actually sees the whole range of SO_2 CDs that occur in the image. This may sometimes require

changing the position of the DOAS FOV within the camera image or adjusting the orientation of the entire SO$_2$ camera-DOAS set-up.

2. The calibration from the DOAS is only valid in the small area where the FOV's of both instruments coincide. Typically this is at -or close to- the centre of the camera image. For the remaining pixels of the image the sensitivity has to be assumed to vary in the same way or has to be characterised, e.g. with calibration cells (see Sect. 4.3). However, if characterised carefully (e.g., in the lab), the DOAS calibration method can eliminate the need to perform calibration cell measurements in the field.

4.3 Non-uniformity of calibration across the field of view

Typically SO$_2$ cameras show an increase in sensitivity toward a given SO$_2$ CD with increasing distance from the optical axis (i.e., the sensitivity increases towards the corners of the image). The AA for a given SO$_2$ CD is influenced by the transmission curve of band-pass interference filters (Kern et al., 2010b). Interference filters show a shift of the filter transmission window towards shorter wavelengths when not illuminated perpendicular. Since the SO$_2$ absorption cross section becomes larger towards shorter wavelengths (e.g., Vandaele et al., 2009), the optical density measured behind Filter A also increases. Because the influence of SO$_2$ on the optical density of Filter B is negligible (also for non-perpendicular illumination) the AA increases considerably for off-centred illumination. As the mean illumination angles at the edges of the detector are larger than at the centre of the image, the AA increases towards the sides of the image. The transmission curve thus changes over the range of the detector depending on the filters chosen and the optical set-up and every camera has to be carefully characterized (more detailed information on the effect of the filter illumination angle and the influence of different optical set-ups can be found in Kern et al., 2010b). The non-uniformity of the response can be eliminated by proper calibration.

4.4 Reflections on the interference filters and gas cells

Radiation arriving at the interference filter is only partly transmitted even at the peak transmission wavelength (we measured peak transmission about $T_A = 64\%$ for Filter A and $T_B = 45\%$ for Filter B). A small fraction is absorbed and a remaining, significant fraction is reflected. If the reflected radiation passes the aperture, part of it is reflected a second time on the windows of the calibration cell. Radiation reflected on the front window of the cell passes the inside of the calibration cell, and therefore the SO$_2$ concentration, two additional times before part of it reaches the detector (see Fig. 2). Since the reflectivity of the two interference filters is different, the reflection effects do not cancel out in the calculation of the AA for a calibration cell image. Without reflection from the interference filter, radiation arriving at the interference filter (with a calibration cell in the light path) can be described by:

$$I(\lambda) = I_0 \cdot e^{-\sigma(\lambda) \cdot S} \cdot (1 - R_Q(\lambda))^4 \tag{4}$$

with the incoming solar radiation I_0, the SO$_2$ cross-section $\sigma(\lambda)$, the SO$_2$ CD S along the light path and the Fresnel reflectivity R_Q at each quartz window of the calibration cell. The exponent of 4 results from the four transitions between quartz glass and air that influence radiation when passing through the calibration cell. Neglecting higher orders reflection terms, i.e., using only radiation that was reflected once at the interference filter and reflected once at one of the different walls of the calibration cell into the direction of the detector and also neglecting the angle dependence of R_Q, we obtain an additional intensity:

$$\Delta I_X(\lambda) = I(\lambda) \cdot R_X(\lambda) \cdot R_Q \cdot \left(\sum_{n=1,2} (1 - R_Q)^{2 \cdot (n-1)} + + \sum_{n=3,4} e^{-2 \cdot \sigma(\lambda) \cdot S} \cdot (1 - R_Q)^{2 \cdot (n-1)} \right) \tag{5}$$

In this equation $R_X = 1 - T_X$ is the reflectivity from the interference filter. The terms for $n = 1,2$ describe reflections on Window 2 in Fig. 2, the terms $n = 3,4$ describe reflection on Window 1. Radiation that is reflected from Window 1 has to pass the inside of the

calibration cell twice, and is influenced by SO_2 absorption. The term $(1 - R_Q)^{2 \cdot (n-1)}$ describes the losses at each quartz glass – air interface. For example, radiation that was reflected from the interference filter passes three interfaces before it is reflected on the outer surface of Window 1 and it passes three additional interfaces before arriving at the interference filter again. Thus, losses for the 6 transitions are accounted for by the term $(1 - R_Q)^6$. Note that reflection on the lens has been neglected because its anti-reflection coating suppresses reflectivity well below that of the calibration cell windows.

A sample calculation for the central wavelengths (CW) of our interference filters will give an estimate of the magnitude of these effects. The CW of our Filter A is 315 nm with a transmission of $T_{A,315\,nm} = 0.64$; the CW of our Filter B is 330 nm with $T_{B,330\,nm} = 0.45$ (both measured in our laboratory). Quartz glass, as used for our calibration cells, has a refractive index of $n = 1.4841$ at 315 nm and $n = 1.4808$ at 330 nm (Interpolated from Heraeus Datasheet, 2011).

The Fresnel equations generally describe the reflection and refraction of radiation at the interface between two different media with refractive indices n_1 and n_2. The reflection coefficients for the polarization plane perpendicular to ($R_\perp$) and parallel to ($R_\parallel$) the plane of incidence are given by:

$$R_\perp = \left(\frac{n_1 \cos\alpha - n_2 \cos\beta}{n_1 \cos\alpha + n_2 \cos\beta} \right)^2 \tag{6}$$

$$R_\parallel = \left(\frac{n_2 \cos\alpha - n_1 \cos\beta}{n_2 \cos\alpha + n_1 \cos\beta} \right)^2 \tag{7}$$

Here α is the incidence angle and β is the refraction angle. For perpendicular ($\alpha = 0$) illumination of the interface between air ($n \approx 1$) and fused silica with unpolarized radiation, the equations can be simplified to:

$$R = \frac{R_\perp + R_\parallel}{2} = \left(\frac{n - 1}{n + 1} \right)^2 \tag{8}$$

We therefore obtain reflection coefficients of $R_A = 3.81 \times 10^{-2}$ (315 nm) and $R_B = 3.76 \times 10^{-2}$ (330 nm) respectively for perpendicular illumination of the calibration cell. These reflection coefficients inserted in Eqs. (3) and (5) lead to $\tau_A = -0.0478$, $\tau_B = -0.0714$ and thus to an AA of -0.0236 (corresponding roughly to an SO$_2$ CD of $\approx 2.4 \times 10^{17}$ molec cm^{-2}) for an empty calibration cell. This means that the AA of a low concentration gas cell recorded at the center of the image could be significantly skewed (by up to the equivalent of ~ 100 ppmm) towards lower values.

In reality the situation is slightly more complex. For one, we do not solely have perpendicular reflection. This leads to an increase in reflectivity (Eqs. 6 and 7). However, most rays that are reflected by the band-pass filter will be blocked by the aperture and will not arrive at the calibration cell again. Of those rays that arrive, only the ones that arrive at the interference filter perpendicular will be reflected to the same position on the detector. In general each ray will be reflected to another position on the detector. Another effect leading to a smaller influence of the reflection is that the reflectivity of the interference filter in general is somewhat less then $R_X = (1 - T_X)$ as a fraction of radiation is absorbed inside the interference filter. The magnitude of the described effect strongly depends on the optical set-up but it will also occur for interference filters that are mounted in front of the lens and any calibration cells that are mounted reasonably parallel to the lens.

4.5 Aerosol influence on the calibration curve

SO$_2$ cameras that use a second filter to correct for plume condensation and aerosols in the volcanic plume usually assume that these effects are independent of wavelength in the region between 305 nm–335 nm. However, both Mie scattering and Rayleigh scattering show a wavelength dependency.

Mie scattering describes the scattering of radiation on particles that have a size comparable to its wavelength. Mie theory is generally complex, but the cross section

for a given wavelength can be estimated as:

$$\sigma_{\text{Mie}}(\lambda) = \sigma_0 \cdot \lambda^{-\alpha} \tag{9}$$

where α is the Ångström exponent (Ångström, 1929, 1961). The Ångström exponent is inversely related to the size of the aerosol particles. Values between 0.13 and 2.42 have, e.g., been found in quiescent degassing volcanic plumes at Mt. Etna (Spinetti and Buongiorno, 2007).

The ratio κ_{Mie} between the scattering cross-sections σ_{Mie} at two different wavelengths λ is then:

$$\kappa_{\text{Mie}} = \frac{\sigma_{\text{Mie},\lambda_1}}{\sigma_{\text{Mie},\lambda_2}} = \left(\frac{\lambda_1}{\lambda_2}\right)^{-\alpha} \tag{10}$$

For Rayleigh scattering (scattering on molecules and particles with a small size compared to the incident wavelength), the ratio κ_{Ray} between the scattering cross-sections $\sigma_{\text{Ray.}}$ at two different wavelengths λ is given by:

$$\kappa_{\text{Ray}} = \frac{\sigma_{\text{Ray},\lambda_1}}{\sigma_{\text{Ray},\lambda_2}} = \left(\frac{\lambda_1}{\lambda_2}\right)^{-4} \tag{11}$$

The effect of radiation being absorbed or scattered out of the camera's FOV on aerosols as it passes through the volcanic plume is wavelength depended. With Eq. (10) we get the relationship between the aerosol optical depths $\tau_{\text{A,aerosol}}$ and $\tau_{\text{B,aerosol}}$ at two wavelengths:

$$\tau_{\text{A,aerosol}} = \tau_{\text{B,aerosol}} \cdot \kappa_{\text{Mie}} \tag{12}$$

The influence on SO_2 camera measurements can be approximated by inserting the central wavelengths of the interference filters used during our experiments ($\lambda_1 = 315\,\text{nm}$ and $\lambda_2 = 330\,\text{nm}$) into Eq. (12). An Ångström Exponent of 1.2 was chosen

as this value is thought to be representative of a typical volcanic plume (Spinetti and Buongiorno, 2007):

$$\tau_{\text{A,aerosol}} = \kappa_{\text{Mie}} \cdot \tau_{\text{B,aerosol}} = 1.057 \cdot \tau_{\text{B,aerosol}} \qquad (13)$$

This indicates that $\tau_{\text{A,aerosol}}$ would be 5.7 % higher than $\tau_{\text{B,aerosol}}$ for a given aerosol
optical density. Therefore aerosols do actually influence the AA, the difference between τ_{A} and τ_{B}, although this is usually neglected.

For a constant aerosol optical density in the volcanic plume the calibration curve would be shifted towards higher AA values. However, it is likely that the AOD increases with increasing SO$_2$ CD. For a linear relationship between SO$_2$ and AOD we obtain a calibration curve with a lower slope (see Fig. 3).

Besides absorption or scattering radiation out of the camera's FOV, volcanic (as well as atmospheric) aerosols also scatter radiation not originating from behind the plume into the camera's FOV. The AA therefore changes, depending on the amount of radiation scattered into the FOV. We will here focus on scattering of radiation on volcanic aerosol. For our sample calculation we assume that the radiation scattered into the camera's FOV from aerosol is proportional to $I_{\text{A/B,M}}$. Geometrical considerations show, that the mean light path length for radiation that was scattered into the camera's FOV from inside the volcanic plume is close to the length of a straight line through the plume assuming a round plume cross-section. The fraction δ of the measurement intensity $I_{\text{B,M}}$ at 330 nm is scattered into the camera FOV. The additional intensity therefore is $\delta \cdot I_{\text{B,M}}$ for Filter B. For Filter A the fraction of additional radiation is different. We have to take into account, that Mie scattering on particles in the plume has different wavelength dependency compared to Rayleigh scattering in the background. This is done by multiplying $\frac{\kappa_{\text{Mie}}}{\kappa_{\text{Rayleigh}}}$. The fraction of additional radiation for Filter A is then $\delta \cdot \frac{\kappa_{\text{Mie}}}{\kappa_{\text{Rayleigh}}}$.

Title Page

Abstract | Introduction

Conclusions | References

Tables | Figures

◄◄ | ►►

◄ | ►

Back | Close

Full Screen / Esc

Printer-friendly Version

Interactive Discussion

$$\tau = \tau_A - \tau_B = -\ln\left(\frac{I_{A,M} \cdot (1 + \delta \cdot \frac{\kappa_{Mie}}{\kappa_{Rayleigh}})}{I_{A,0}}\right) + \ln\left(\frac{I_{B,M} \cdot (1 + \delta)}{I_{B,0}}\right)$$

$$= \tau_{SO_2} + \underbrace{\ln\left(\frac{1 + \delta}{1 + \delta \cdot \frac{\kappa_{Mie}}{\kappa_{Rayleigh}}}\right)}_{\Delta\tau} \tag{14}$$

Since $\frac{\kappa_{Mie}}{\kappa_{Rayleigh}}$ is less then one there is a shift of the calibration curve towards higher AA values if radiation is scattered into the FOV by Mie-scattering (note: the DOAS technique is not affected by this since broad band structures are removed in the DOAS evaluation). For an Ångström exponent of 1.2 and $\delta = 0.2$ we obtain $\Delta\tau = 0.0206$, with the CWs of the Filters used during this work. This roughly corresponds to an SO$_2$ CD of 2.5×10^{17} molec cm^{-2} or ~ 100 ppmm.

5 Data acquisition and evaluation

5.1 SO$_2$ camera

The SO$_2$ camera acquired images with both filters sequentially: exposure times were adjusted to keep the maximum measured intensity signal at about 85 % of the maximum intensity (65 536 counts with the 16 bit ADC). Before and after each measurement period, the camera was pointed towards a region of the sky free of clouds and volcanic gas (if available), to obtain background images for both filters. Normalization with the background images removes vignetting from the camera images, as this effect occurs both in the background as well as in the measurement images. Whenever background images were acquired, images with the calibration cells inserted into the light path and reference spectra for the DOAS evaluation were also recorded.

As a first evaluation step all camera images were corrected for offset and dark current by subtracting a dark image. Next, the background images I_0 are scaled such that the average intensity in a gas-free subsection of the plume images I_M match the average intensity in the same subsection of the respective background images. We obtain normalised intensities $I_{A,0}^*$, $I_{B,0}^*$:

$$I_{A,0}^* = c_A \cdot I_{A,0} \tag{15}$$

$$I_{B,0}^* = c_B \cdot I_{B,0} \tag{16}$$

with

$$c = \frac{\bar{I}_M^{\text{Clear Sky}}}{\bar{I}_0^{\text{Clear Sky}}} \tag{17}$$

The optical density for each filter is then calculated from the plume images $I_{A,M}$ and $I_{B,M}$, and scaled background images $I_{A,0}^*$ and $I_{B,0}^*$:

$$\tau_A = -\ln \frac{I_{A,M}}{I_{A,0}^*} \tag{18}$$

$$\tau_B = -\ln \frac{I_{B,M}}{I_{B,0}^*} \tag{19}$$

Inserting this in Eq. (3) we obtain the AA:

$$\tau = -\ln \frac{I_{A,M}}{I_{A,0}^*} + \ln \frac{I_{B,M}}{I_{B,0}^*} \tag{20}$$

Calibration of the SO$_2$ camera

P. Lübcke et al.

For the comparison with the CD obtained by the IDOAS and the calculation of the SO$_2$ fluxes all AA images were corrected for higher sensitivity towards the edges of the detector (Sect. 4.3). A 2nd order polynomial was fitted to calibration cell images, not considering areas affected by reflections (Sects. 4.4 and 6.2). From these fits a reflection free AA image was simulated. The AA was normalised to 1 in the area were the DOAS telescope is pointing. Higher sensitivity towards the edges of the detector was corrected by dividing each pixel of the AA images by the corresponding pixel of the mask.

5.2 Spectroscopic retrieval

The spectra recorded with the two spectrometers (NFOV-DOAS, IDOAS) were evaluated using the DOASIS software package (DOASIS: Kraus, 2006). The standard DOAS retrieval was applied in the wavelength range between 314 nm and 326 nm (e.g., Platt and Stutz, 2008). The absorption cross-sections of SO$_2$ (298K, Vandaele et al., 2009) and O$_3$ (both 221 K and 241 K, Burrows et al., 1999) were fitted to the measurement spectra along with a Fraunhofer reference spectrum (measured away from the plume in close time proximity) and a Ring spectrum (calculated from the Fraunhofer reference Grainger and Ring, 1962). All cross sections were convoluted to the instrument resolution using the measured instrument response to the 334.15 nm line of a mercury emission lamp. To correct for small inaccuracies in the pixel-wavelength-mapping, e.g., due to slight changes in the instrument's temperature, the Fraunhofer reference spectrum linked together with the Ring spectrum was allowed to be slightly shifted and squeezed against the measurement spectrum during the DOAS evaluation. All reference cross sections were also allowed to be shifted and squeezed together as a set. A maximum shift of ±0.2 nm and squeeze of ±2 % were allowed in both cases.

The DOAS fit for the IDOAS data was performed individually for each pixel using the same evaluation scheme as for the other spectroscopic data. As the instrument's slit function varies over the detector, the cross sections were individually convoluted for each row of the detector. Due to problems with data logging, no exposure times were

available for the IDOAS. Spectra were therefore only corrected for offset. However, later measurements determined that the dark current at the same detector temperature can be considered below 0.1 % of the signal for exposures times of approximately 3 s, and is therefore negligible.

5.3 Viewing direction of the DOAS telescope

The data from the NFOV-DOAS together with the corresponding AA data from the SO_2 camera were used to create a calibration curve. It is important to exactly know the area to which the DOAS telescope is directed. We measured the viewing direction of the telescope relative to the camera by coupling light from a halogen lamp into the spectrometer side of the optical fibre in our laboratory. We then acquired images with the camera to determine the position of the light spot on a wall in the camera image.

However, after the measurements were completed, we found that the FOV had changed during the transport to the measurement site. Therefore we estimated the size of the FOV and viewing direction of the telescope by searching for the best correlation between AA time-series recorded by the SO_2 camera and SO_2 CD time-series recorded by the NFOV-DOAS as described in Kern et al. (2010b). We applied this technique with a few minor changes. Instead of quadratic sectors, we chose a round FOV to better approximate the true FOV of the DOAS telescope.

The radius of the FOV was varied and for each radius, the FOV was shifted across the camera image. For each position an AA time series was created by calculating the mean AA value in the FOV as a function of time. As the acquisition time of the spectrograph generally is different from the acquisition time for the camera, the AA time series obtained from the camera images was interpolated to match the acquisition times of the DOAS spectra. After the time interpolation, the linear correlation between the AA time series and the SO_2 CD time series from the DOAS was calculated. This way we obtained the radius with the best correlation, and a "correlation map" that shows where the correlation between the camera's AA time-series and the DOAS's SO_2 CD time-series has its maximum. Although a stable design of the camera-NFOV-DOAS

assembly and laboratory calibration are preferable, we recommend checking of the relative alignment by the method described above.

5.4 Comparison between SO$_2$ camera and IDOAS

The SO$_2$ camera and the IDOAS differ in temporal and spatial resolutions. While the SO$_2$ camera acquires an AA image approximately every 3 to 4 s with a quadratic FOV of roughly 22° by 22°, the IDOAS needs between 5 and 25 s to acquire one column of the image with a FOV of 13° (vertically) × 0.26° (horizontally). For example, the image that we will discuss in this paper was recorded between 10:30 a.m. and 11:15 a.m. on 4 March 2011. It has a spatial extension of 13° (vertically) × 44.5° (horizontally). The SO$_2$ camera recorded 815 AA images during this time period. The data obtained from the two instruments were carefully prepared to be comparable. As a first step, a transformation matrix was created to translate, rotate, shear and scale the SO$_2$ camera images to the IDOAS FOV. This was done by manually choosing feature points (e.g. vent of the volcano) that can be distinguished in both the SO$_2$ camera image and in the IDOAS image. This set of points was used to create the image transformation matrix. After the matrix was applied to all camera images, the images matched a sub-section of the IDOAS FOV (since the IDOAS image has a larger horizontally FOV than the SO$_2$ camera). The acquisition start and end time is known for each column of the IDOAS: for the corresponding image constructed from SO$_2$ camera measurements, we used the average of all camera images recorded between the start and end time to construct the corresponding column for comparison.

6 Field measurements: set-up and results

6.1 The measurement set-up at Popocatépetl

Measurements from three days (1, 2 and 4 March 2011) will be discussed here. For clarity, these days will be referred to as Day 1, Day 2 and Day 3, respectively, in the rest

of the text. Measurements were performed from the rangers post at Paso de Cortés (longitude: −98.64694, latitude: 19.0867), approximately 7 km north of the volcano's vent. The viewing direction of the camera and the solar azimuth angle are shown in the top row of Fig. 4, for the start and end times of measurements. The red line indicates the viewing direction used for calibration cell and background image acquisition. Photos giving an impression of the measurement conditions during the three measurement days are shown in the bottom row of Fig. 4. During all measurements, background images and calibration cell images were acquired before and after measurements if an area of clear sky was available. The results will be discussed and interpreted in this chapter. All calibration cell measurements, presented here, were performed in the morning hours (between 09:30 a.m. and 11:00 a.m. local time) with approximately the same viewing direction. Additional car traverses were performed with a zenith-looking DOAS instrument to determine the wind-direction. Usually, however, the car traverses were not conducted at the same time as camera measurements.

6.2 General results from calibration cells

Figure 5 a shows the AA of a calibration cell with an SO_2 CD of 1.77×10^{18} molec cm^{-2}. The image was created by applying Eq. (3) to images taken in the background geometry with the calibration cell covering the entire field-of-view. As the viewing direction does not change, no normalisation (Eq. 17) is necessary, i.e., $c_A = c_B = 1$. Two features can be seen in Fig. 5 a: first, a clear increase in signal with increasing distance from the centre of the image can be observed. We see an increase in AA of up to 85 % between the centre, where AA is lowest, and the corners of the detector, where the AA is highest.

The second feature that can be seen in Fig. 5a is a (slightly off-centre) ring like structure (arrows) in the middle of the AA image of the calibration cell. This feature can be attributed to reflections on the windows of the calibration cell (Sect. 4.4).

Figure 5b shows an AA image that was created by fitting two-dimensional 2nd order polynomials to the variation of intensity of the calibration cell raw images, without

Full Screen / Esc

Printer-friendly Version

Interactive Discussion

considering the area affected by the reflection features. These polynomial fits were then used to create AA images without reflection structures. Camera images used in the comparison with IDOAS and for the SO$_2$ fluxes are corrected for higher sensitivity towards the edges of the image by applying a correction matrix created from AA images created in this manner.

Figure 5c shows τ_B from a calibration cell measurement: a circular structure can be observed in the centre of the image, where the optical density is lower, i.e., more radiation arrives in the centre of the detector than at the rest of the detector. As the intensity seen through Filter B is essentially unaffected by SO$_2$ absorption we would expect a flat signal over the complete detector. However, reflections on the calibration cell windows cause additional radiation to be reflected into the center of the image (see Fig. 2).

6.3 Results from the field measurements

6.3.1 Calibration

The FOV of the DOAS instrument within the SO$_2$ camera image had to be derived for the DOAS calibration (see Sect. 5.3). The best correlation between the SO$_2$ CD time-series and the AA time-series was found for a circle with a radius of 57 pixels. Small changes in the viewing direction result in small variations of the correlation coefficient (see Fig. 6). Differences in the area with best correlation were found to be very low (on the order of 0.2°) between the different days thus indicating that the pointing of the DOAS telescope in relation to the camera optics had not changed. However we found changes of the slope of the calibration curve of up to 8 % when fitting a first order polynomial in an area that includes correlation coefficient values within 1 % of the maximum. (Data from Day 3 was not included in these estimates as there was a slight deviation from linear behaviour, see Sect. 6.3.4). Also, the offset for first order calibration polynomial varied between -2.2×10^{17} molec cm^{-2} and 1.5×10^{17} molec cm^{-2} across this area. In future measurements, the uncertainty arising from the viewing direction of

the DOAS telescope should be reduced by exactly measuring the DOAS FOV at the measurement site.

For calibration with cells, the calibration curves obtained during the three days (see Sects. 6.3.2, 6.3.3 and 6.3.4) differ very little for all of the measurements. The slope of linear fits to the calibration cell AA/SO_2 CD pairs varied by only about $\sim 1\%$ during the entire measurement period. This indicates that the instrument was very stable and exhibited a nearly constant sensitivity towards SO_2 calibration cells (at close proximity to the instrument).

6.3.2 Day 1, 1 March 2011

On this day, the calibration curves from the calibration cells and the DOAS both show a linear relationship between AA and CD (Fig. 7). The DOAS measurements correlate very well with the camera's apparent absorption time series (R^2 of 0.978). However the slopes derived by the two calibration methods differ by almost 20%.

The optical densities τ_A and τ_B obtained for the two filters (Fig. 8) each also show a linear dependency on the DOAS-derived SO_2 CD. While τ_A exhibits the expected increase in magnitude with increasing SO_2 load due to absorption, τ_B actually decreases with increasing SO_2 CD. This can be explained by light being scattered toward the instruments on aerosol and cloud droplets that are generally co-located with areas of high SO_2 CD. Thus, the plume appears slightly brighter than the background at 330 nm, where SO_2 absorption is negligible.

Figure 9 shows the NFOV-DOAS time series in comparison to the SO_2 camera time series (average of the AA for all pixels coinciding with the DOAS FOV) from Day 1. After converting the AA to SO_2 column densities by multiplying with the calibration factor of 9.58×10^{18} molec cm^{-2} obtained from the DOAS (see Fig. 7, the offset was also taken into account), 95% of the DOAS measurement values lie within $\pm 1.5 \times 10^{17}$ molec cm^{-2} of the camera data points.

6.3.3 Day 2, 2 March 2011

AA values derived in the DOAS FOV again show very good correlation with the DOAS derived SO_2 CDs on Day 2 (see Fig. 10). This time the calibration curves derived from the DOAS and the calibration cells show better agreement: they differ only by about 5.6 % and the offset between the two calibration curves is only 3×10^{16} molec cm^{-2}. The measurements show that the linear relationship between AA and SO_2 CD holds true for up to 4×10^{18} molec cm^{-2} (approx. 1600 ppmm) in this case. Figure 11 shows the individual optical densities $\tau_{A/B}$ for Filter A and Filter B. While the slope for τ_A is comparable to Day 1, the slope of τ_B is much steeper than on Day 1, i.e., there is less change of τ_B with changing SO_2 CD, likely indicating a smaller aerosol load in the plume on this day.

6.3.4 Day 3, 4 March 2011

On 4 March 2011 two time-series were recorded, one between 09:15 a.m. and 10:00 a.m. the other between 10:38 a.m. and 11:45 a.m. From 09:15 a.m. until 09:36 a.m., the DOAS calibration curve is similar to Day 1 (Fig. 12). This time interval will hence be referred to as "Part 1". For the rest of the measurements, however, the calibration curve deviates slightly from a linear relationship. For increasing SO_2 CDs all data points are shifted towards higher AA values compared to the calibration cells (Fig. 13). This interval will be referred to as "Part 2". Figure 14 shows both time series. Calibration for this figure was performed with the green NFOV-DOAS curve from earlier in the day (Part 1, Fig. 12). Calibrated in this way, the camera overestimates the SO_2 column densities in Part 2 when compared with the DOAS for high SO_2 CDs.

The SO_2 CDs are plotted as a function of the optical densities for Filter A and B in Fig. 15. The optical densities τ_A and τ_B for Part 1 show similar behaviour as on Day 1. For Part 2 most data points are shifted towards higher optical densities.

Simultaneous Imaging DOAS (IDOAS) measurements (taken between 10:38 a.m. and 11:45 a.m. on Day 3) were used to further investigate the calibration. Comparing

the images constructed from the camera images (see Sect. 5.4) and the IDOAS measurement (Fig. 16), the overall structure of the volcanic plume appears similar in both images. A noteworthy fact is that the camera image seems to have SO$_2$ columns of up to 2×10^{17} molec cm^{-2} in areas where the IDOAS shows no enhanced SO$_2$. This effect is caused by changes in the the background intensity over the field of view of the SO$_2$-camera. Due to the sun's azimuthal position (approximately in line with the azimuthal viewing direction of the camera, see Fig. 4), the ratio between the scattered radiation intensity at 315 nm and 330 nm is not constant over the entire image.

To further compare the calibrations we reduced the image size to 127 (horizontally) × 88 (vertically) pixels to reduce errors caused by imperfect image alignment. All values that were below a thresholds of 1.5×10^{17} molec cm^{-2} for IDOAS measurements and below 0.01 AA for camera images were removed. The remaining data points were used to create a calibration curve that can be compared with the calibration curve obtained from the DOAS instrument incorporated in our camera. The result in Fig. 13 shows that the calibration curve we obtained with our NFOV-DOAS instrument is in general agreement with the IDOAS measurements. The calibration obtained from the IDOAS is slightly more noisy, probably due to an imperfect spatial and temporal alignment. Since the SO$_2$ camera images were spatially transformed to match the IDOAS FOV and averaged to match the IDOAS time resolution, small errors due to misalignment are possible. Both calibration curves clearly deviate from the calibration cell measurements for AA values above 0.1.

6.4 Discussion of calibration results

On all days the optical density for Filter B decreased with increasing SO$_2$ column density. This shows that more radiation is incident at 330 nm from areas with high SO$_2$ column densities compared to the background intensity, an indication for radiation being scattered on volcanic aerosol into the camera's FOV. Comparing the optical density τ_B for Day 1 and 2 (Figs. 8 and 11) one can see that τ_B has a smaller slope on Day 1 compared to Day 2, possibly due to a higher abundance of volcanic aerosol

on Day 1. However, the measurement geometry shown in Fig. 4 also shows that the relative azimuth between the viewing direction of the camera and the sun's position is smaller on Day 1 compared to Day 2. Since forward scattering is dominant in Mie-scattering, a larger fraction of radiation might have been scattered into the camera's FOV by aerosols and condensed water in the plume. As discussed in Sect. 4.5, Mie scattered radiation leads to an increase in AA and therefore to a decrease of the calibration curve. Comparing Figs. 7 and 10 shows that the slope of the calibration curve on Day 1 is indeed lower, as expected for a higher aerosol influence.

On Day 3 the situation is more complex. Between 09:15 a.m. and 09:36 a.m. (Part 1), both optical densities τ_A and τ_B and the AA behave similar to Day 1, indicating some radiation scattered into the camera's FOV (Figs. 12 and 15).

For Part 2, both optical densities are shifted towards higher values compared to Part 1 (Fig. 15). Less radiation is arriving at the camera's detector for both wavelength channels, which could be caused by more absorbing aerosol in the volcanic plume. τ_B still shows lower values with increasing SO$_2$ CDs, indicating that besides aerosol absorption some radiation is still scattered into the FOV by volcanic plume aerosol and/or condensed water.

6.5 SO$_2$ fluxes

In order to test the influence of the calibration on the retrieved SO$_2$ emission rate, SO$_2$ fluxes for both calibration methods were determined the following manner: first, all AA values were converted to SO$_2$ column densities using calibration curves derived from both the DOAS and from the calibration cells (see Figs. 7, 10, 12 and 13).

As measurements were performed at a distance L of 6–8 km from the volcanic plume, the measured SO$_2$ CD is influenced by the radiation dilution effect (Kern et al., 2010a). A correction for this effect as suggested in Bluth et al. (2007) and Vogel et al. (2011) was applied to the column densities S such that:

$$S(L) = S_0 \cdot e^{-\epsilon \cdot \Delta L} \tag{21}$$

ϵ is an extinction coefficient and depends on the physical state of the atmosphere. We used a value of $\epsilon = 0.057\,km^{-1}$ which was derived by Vogel et al. (2011) for a wavelength of 315.4 nm for measurements of the plume of Popocatépetl under comparable conditions. However, due to the difference in measurement set-ups between our study and that of Vogel et al. (2011) (especially regarding the altitude of the detector), this extinction coefficient represents a lower boundary for the influence of the radiation dilution effect. Solving Eq. (21) for S_0 therefore yields a conservative estimate of the SO$_2$ CD in the plume.

Next we summed SO$_2$ CDs up along a cross-section of the plume. The cross-section ideally is perpendicular to the propagation direction of the plume. However, as explained in Mori and Burton (2006) non-perpendicular viewing direction cancels out in the calculation of the flux if the wind speed is derived from the camera data (see below), since both the derived wind-speed and the SO$_2$ column density are a function of the viewing direction. In integrating along a plume cross-section we summed up all pixels with column densities exceeding the background noise ($\approx 1\text{--}2 \times 10^{17}$ molec cm^{-2}, determined in areas of the pictures not covered by the volcanic plume). This was done for two parallel cross-sections with a difference in azimuth angle of approximately 2°. Cross-correlations of time series of the integrated SO$_2$ column densities were used to determine the time required for SO$_2$ to travel between the two positions (see e.g. Johansson et al., 2009; Boichu et al., 2010). We used a correlation window of roughly 600 s and obtained very good correlation between the time-series of the two cross-sections (usually the correlation coefficient was 0.9 or better) with time lags typically between 28 and 35 s.

Wind directions were interpolated from the READY NOAA database (READY, GDAS data) at an estimated plume altitude of 5500 m. The uncertainty of the modelled wind directions was assessed by comparing wind directions determined by car traverses at a later time of day to modelled wind directions for the same time. Measurements and modelled wind directions differed by on average 10.6°, with a maximum difference of

Full Screen / Esc

Printer-friendly Version

Interactive Discussion

18°. This greatest deviation was used to find the uncertainty of the distance between the two integrated cross-sections using error propagation.

The distance between the two cross-sections was calculated from the angle between them and the distance between the instrument and the volcanic plume. The thus obtained wind-speed v represents the wind-speed perpendicular to the viewing direction.

We then calculated the flux as:

$$\Phi = v \cdot \sum \Delta h_i \cdot S_0(\tau_i) \tag{22}$$

where Δh_i is the height that one pixel represents at the location of the plume. This was calculated from the distance to the plume and the solid angle covered by one pixel given the camera's object lens.

For a constant calibration factor c the flux becomes:

$$\Phi = v \cdot c \cdot e^{c \cdot \Delta L} \cdot \sum \Delta h_i \cdot \tau_i \tag{23}$$

The dominating sources of uncertainty during our measurements were the calibration (uncertainty of 8 % for 1 and 2 of March 2011, as explained in Sect. 6.3 and uncertainties in the wind-speed (about 10 %, dominated by the uncertainty of the cross-correlation of the time series). Therefore, the total measurement uncertainty of the SO_2 flux can be estimated as:

$$\Delta \Phi = \sqrt{(\frac{\partial \Phi}{\partial v} \cdot \Delta v)^2 + (\frac{\partial \Phi}{\partial c} \cdot \Delta c)^2} \tag{24}$$

On 1 March 2011 we thus obtained radiation dilution corrected fluxes ranging between $4.45 \pm 0.66\,\mathrm{kg\,s^{-1}}$ and $22.64 \pm 3.9\,\mathrm{kg\,s^{-1}}$, with a mean flux of $10.56\,\mathrm{kg\,s^{-1}}$ (see Fig. 17).

On Day 2 and 3 our SO_2 fluxes only represent a lower limit, since the plume was partly moving in front and behind Popocatépetl and we could only partly detect the gas

Full Screen / Esc

Printer-friendly Version

Interactive Discussion

emissions. Mean fluxes for all measurement periods with both calibration methods are shown in Table 2. While the SO$_2$ camera calibrated with cells can measure the SO$_2$ flux correctly under favourable conditions (only 6 % difference on 2 March 2011), differences in the flux of up to 25 % occurred (4 March 2011) when aerosols and condensed water in the volcanic plume significantly influenced the calibration.

7 Conclusions

In this study we compared different methods for calibrating SO$_2$ camera systems and investigated possible errors associated with them. While arguably the most straightforward method, calibrating the SO$_2$-sensitivity of UV cameras by placing cells of known concentration in the optical path has some drawbacks. We found that reflections on the calibration cell windows can influence the measured AA and can therefore have a detrimental effect on the calibration. During cell calibration with our instrument, circular structures could be observed in the image centre, a result of multiple reflections on the calibration cell windows. While this effect could potentially be avoided by introducing the cells into the optical path at a non-perpendicular angle, this approach would introduce further complications. The sensitivity of UV cameras is known to vary over the extent of the image (e.g., Kern et al., 2010b), with these variations typically being a function of distance to the image centre. Positioning calibration cells at an angle would introduce an additional component, as the observed cell thickness would then vary across the detector in a non-radial manner. The exact behaviour would depend on the cell placement in or in front of the optical system, but correcting for both effects simultaneously certainly increases complexity and is more prone to errors.

We could show that the cell calibration can give misleading results since it can not account for changes in camera sensitivity due to the presence of aerosol in the plume as is explained below. Calibration with a co-located DOAS system, on the other hand, worked well. We showed how the correlation between the time series of DOAS column densities and that of the camera's AA values can be used to obtain an accurate

estimation of the spectrometer's field of view within the camera image. However, in a sensitivity study, the camera calibration was found sensitive to the exact size, shape and position of the assumed DOAS FOV. Therefore, accurate characterization of these parameters is key in obtaining the best possible camera calibration, and any variation in the exact position of the FOV over time should be avoided. Comparison with the Imaging DOAS, although slightly more complicated due to the stark difference in image acquisition time (20 min as opposed to 2 s), was encouraging and showed that the NFOV-DOAS calibration curve derived in the centre of the image can indeed be used across the entire image as long as the radial variation in camera sensitivity is accounted for.

Besides eliminating the need for manual placement of cells or motorized moving parts in the camera design, integrating a DOAS spectrometer into the camera system also yielded the possibility to assess the influence of volcanic aerosols on the camera calibration. We found that radiation scattered into the camera's field of view on aerosols and condensed water in a volcanic plume can lead to a change in the sensitivity of the camera towards SO$_2$. Even though no significant change in the camera's calibration between the three discussed days could be determined with the calibration cell method, the DOAS-derived calibration curves varied significantly. While the difference between cell and DOAS calibration slope was only 6 % under favorable conditions, deviations of up to 60 % were found on 4 March 2012 when a combination of plume aerosol conditions and illumination and viewing geometry led to significant aerosol scattering and absorption effects – effects that are not accounted for when calibrating with a gas cell.

Even in the conditions encountered here, where moderate SO$_2$ column densities (below $\sim$ 2000 ppmm) were found and the volcanic plume was generally translucent, the DOAS-derived calibration will be considerably more accurate than calibrating with cells. It is important to keep in mind, however, that aside from applying an empirical distance correction, the complex radiative transfer of the scene has not been dealt with explicitly. Therefore, this method will also fail in the case of very high SO$_2$ column

densities ($\sim$ several thousand ppmm) and visibly opaque plumes. In such conditions, taking complex radiative transfer into account in an explicit manner when evaluating the DOAS data would be necessary (Kern et al., 2012b). In combination with a sophisticated DOAS retrieval technique, the integration of a DOAS spectrometer into the camera instrument would then allow a reasonable estimate of SO_2 distributions, even under extreme SO_2 conditions and highly opaque plumes.

After the SO_2 camera data was consistently calibrated with the DOAS, a significant variability in the SO_2 emission rate was still found. We measured average SO_2 emission rates from Popocatépetl Volcano of between 4 and 14.3 kg s^{-1} for the three days of observation. Although the plume was not always in full sight and these values therefore represent conservative estimates, the variability in emission rates was also apparent when the plume was in full view, as was the case on 1 March 2011. On this day alone, emission rates ranged from 4.5 and 23 kg s^{-1}, with large variations occurring on time scales of minutes.

This high variability of SO_2 emissions at Popocatépetl Volcano is not unique and has in fact been observed at many other volcanoes around the world. Although the processes that cause this variability are not yet well understood, the SO_2 camera for the first time allows us to capture these fluctuations at high temporal resolution. It therefore represents a very promising technique for volcano monitoring and systems research. However, we have shown that the accuracy of such UV imaging instrumentation is significantly determined by the ability to obtain an accurate calibration with regard to SO_2 sensitivity. For this, the integration of a narrow field of view DOAS spectrometer is of immense value. It enables a dynamic calibration under the actual measurement conditions, avoids technical issues associated with placing gas cells into the light path, allows the identification of aerosol scattering effects, and can therefore be considered a key element in the SO_2 camera system.

Appendix A

Simulation of the AA from a measured solar radiation spectrum

The AA for a given SO$_2$ column density was simulated and shown in Fig. 3. A solar spectrum $I(\lambda)$ measured at the measurement site with the spectrograph was used in the simulation. Besides the incident radiation, the signal at the detector is also influenced by the transmission curves of our band-pass interference filters $T_A(\lambda)$, $T_B(\lambda)$, the quantum efficiency $Q(\lambda)$ of the detector and by potential SO$_2$ absorption. The extinction due to SO$_2$ absorption is given by the absorption cross-section $\sigma(\lambda)$, the column density S. and the Beer-Lambert law of absorption. Therefore, the AA τ can be simulated using the equation:

$$\tau = -\ln\left(\frac{\sum_\lambda I(\lambda) \cdot T_A(\lambda) \cdot Q(\lambda) \cdot \exp(-\sigma(\lambda) \cdot S)}{\sum_\lambda I(\lambda) \cdot T_A(\lambda) \cdot Q(\lambda)}\right) + \ln\left(\frac{\sum_\lambda I(\lambda) \cdot T_B(\lambda) \cdot Q(\lambda) \cdot \exp(-\sigma(\lambda) \cdot S)}{\sum_\lambda I(\lambda) \cdot T_B(\lambda) \cdot Q(\lambda)}\right) \quad \text{(A1)}$$

We used the SO$_2$ absorption cross-section σ from Vandaele et al. (2009) and estimated the quantum effiency Q from the Apogee Alta U6 data-sheet. The filter transmission curves τ_A and τ_B were measured in our laboratory (the transmission curves for perpendicular illumination were used in the calculations).

Title Page

Abstract | Introduction

Conclusions | References

Tables | Figures

|◄ | ►|

◄ | ►

Back | Close

Full Screen / Esc

Printer-friendly Version

Interactive Discussion

References

Ångström, A.: On the Atmospheric Transmission of Sun Radiation and on Dust in the Air, Geogr. Ann. A, 11, 156–166, 1929. 6199

Ångström, A.: Techniques of Determinig the Turbidity of the Atmosphere, Tellus A, 13, 214–223, 1961. 6199

Bluth, G. J. S., Shannon, J. M., Watson, I. M., Prata, A. J., and Realmuto, V. J.: Development of an ultra-violet digital camera for volcanic SO_2 imaging, J. Volcanol. Geoth. Res., 161, 47–56, doi:10.1016/j.jvolgeores.2006.11.004, 2007. 6188, 6211

Bobrowski, N., Hönninger, G., Lohberger, F., and Platt, U.: IDOAS: A new monitoring technique to study the 2D distribution of volcanic gas emissions, J Volcanol. Geoth. Res., 150, 329–338, doi:10.1016/j.jvolgeores.2005.05.004, 2006. 6192

Boichu, M., Oppenheimer, C., Tsanev, V., and Kyle, P. R.: High temporal resolution SO_2 flux measurements at Erebus volcano, Antarctica, J. Volcanol. Geoth. Res., 190, 325–336, doi:10.1016/j.jvolgeores.2009.11.020, 2010. 6186, 6212

Burrows, J. P., Richter, A., Dehn, A., Deters, B., Himmelmann, S., Voigt, S., and Orphal, J.: Atmospheric remote-sensing reference data from GOME-2. Temperature-dependent absorption cross-sections of O_3 in the 231–794 nm range, J. Quant. Spectrosc. Ra., 61, 509–517, 1999. 6203

Dalton, M. P., Watson, I. M., Nadeau, P. A., Werner, C., Morrow, W., and Shannon, J. M.: Assessment of the UV camera sulfur dioxide retrieval for point source plumes, J. Volcanol. Geoth. Res., 188, 358–366, doi:10.1016/j.jvolgeores.2009.09.013, 2009. 6187, 6188, 6192, 6193

Dalton, M. P., Waite, G. P., Watson, I. M., and Nadeau, P. A.: Multiparameter quantification of gas release during weak Strombolian eruptions at Pacaya Volcano, Guatemala, Geophys. Res. Lett., 37, L09303, doi:10.1029/2010GL042617, 2010. 6187

Galle, B., Johansson, M., Rivera, C., Zhang, Y., Kihlman, M., Kern, C., Lehmann, T., Platt, U., Arellano, S., and Hidalgo, S.: Network for Observation of Volcanic and Atmospheric Change (NOVAC): A global network for volcanic gas monitoring: Network layout and instrument description, J. Geophys. Res., 115, D05304, doi:10.1029/2009JD011823, 2010. 6185, 6186

Grainger, J. F. and Ring, J.: Anomalous Fraunhofer Line Profiles, Nature 193, 762, doi:10.1038/193762a0, 1962. 6203

Heraeus Spectrosil©2000 Datasheet, HQS-SO Spectrosil: available at: http://optik.heraeus-quarzglas.de/media/webmedia_local/downloads/Spectrosilsyntheticfusedsilica.pdf (last access: 29 August 2012), May 2012. 6197

Holland, A. S. P., Watson, I. M., Phillips, J.-C., Caricchi, L., and Dalton, M. P.: Degassing processes during lava dome growth: Insights from Santiaguito lava dome, Guatemala, J. Volcanol. Geoth. Res., 202, 153–166, doi:10.1016/j.jvolgeores.2011.02.004, 2011. 6192

Johansson, M., Galle, B., Zhang, Y., Rivera, C., Chen, D., and Wyser, K.: The Dual-Beam mini-DOAS technique – measurements of volcanic gas emission, plume height and plume speed with a single instrument, B. Volcanol., 71, 747–751, doi:10.1007/s00445-008-0260-8, 2009. 6186, 6212

Kantzas, E. P., McGonigle, A. J. S., Tamburello, G., Aiuppa, A., and Bryant R. G.: Protocols for UV camera volcanic SO_2 measurements, J. Volcanol. Geoth. Res., 194, 55–60, 2010. 6187, 6188, 6192

Kern, C., Deutschmann, T., Vogel, L., Wöhrbach, M., Wagner, T., and Platt, U.: Radiative transfer corrections for accurate spectroscopic measurements of volcanic gas emissions, B. Volcanol., 72, 233–247, doi:10.1007/s00445-009-0313-7, 2010a. 6186, 6187, 6194, 6211

Kern, C., Kick, F., Lübcke, P., Vogel, L., Wöhrbach, M., and Platt, U.: Theoretical description of functionality, applications, and limitations of SO2 cameras for the remote sensing of volcanic plumes, Atmos. Meas. Tech., 3, 733–749, doi:10.5194/amt-3-733-2010, 2010b. 6188, 6190, 6191, 6194, 6195, 6204, 6214

Kern, C., Werner, C. A., Doukas, M. P., Elias, T., Kelly, P. J., and Sutton, A. J.: Imaging volcanic SO_2 plumes with UV cameras, Geophys. Res. Abstr., EGU2012-12596, EGU General Assembly 2012, Vienna, Austria, 2012a. 6187

Kern, C., Deutschmann, T., Werner, C., Sutton, A. J., Elias, T., and Kelly, P. J.: Improving the accuracy of SO_2 column densities and emission rates obtained from upward-looking UV-spectroscopic measurements of volcanic plumes by taking realistic radiative transfer into account, J. Geophys. Res., in review, 2012b. 6216

Kraus, S. G.: DOASIS, A Framework Design for DOAS, Ph.D. thesis, University of Mannheim, 2006. 6203

Lohberger, F., Hönninger, G., and Platt, U.: Ground-Based Imaging Differential Optical Absorption Spectroscopy of Atmospheric Gases, Appl. Optics, 43, 4711–4717, 2004. 6192

Calibration of the SO$_2$ camera

P. Lübcke et al.

Title Page

Abstract | Introduction

Conclusions | References

Tables | Figures

|◄ | ►|

◄ | ►

Back | Close

Full Screen / Esc

Printer-friendly Version

Interactive Discussion

Louban, I., Bobrowski, N., Rouwet, D., Inguaggiato, S., and Platt, U.: Imaging DOAS for volcanological applications, B. Volcanol., 71, 753–765, doi:10.1007/s00445-008-0262-6, 2009. 6190, 6192, 6193

McGonigle, A. J. S., Inguaggiato, S., Aiuppa, A., Hayes, A. R., and Oppenheimer, C.: Accurate measurement of volcanic SO_2 flux: Determination of plume transport speed and integrated SO_2 concentration with a single device, Geochem. Geophy. Geosy., 6, Q02003, doi:10.1029/2004GC000845, 2005. 6186

McGonigle, A. J. S., Aiuppa, A., Ripepe, M., Kantzas, E. P., and Tamburello, G.: Spectroscopic capture of 1 Hz volcanic SO_2 fluxes and integration with volcano geophysical data, Geophys. Res. Lett., 36, L21309, doi:10.1029/2009GL040494, 2009. 6186

Moffat, A. J. and Millan, M. M.: The applications of optical correlation techniques to the remote sensing of SO_2 plumes using sky light, Atmos. Environ., 5, 677–690, 1971. 6185

Mori, T. and Burton, M.: The SO_2 camera: A simple, fast and cheap method for ground-based imaging of SO_2 in volcanic plumes, Geophys. Res. Lett., 33, L24804, doi:10.1029/2006GL027916, 2006. 6187, 6188, 6192, 6212

Mori, T. and Burton, M.: Quantification of the gas mass emitted during single explosions on Stromboli with the SO_2 imaging camera, J. Volcanol. Geoth. Res., 188, 395–400, ISSN 0377-0273, doi:10.1016/j.jvolgeores.2009.10.005, 2009. 6187

Nadeau, P. A., Palma, J. L., and Waite, G. P.: Linking volcanic tremor, degassing, and eruption dynamics via SO_2 imaging, Geophys. Res. Lett., 38, L01304, doi:10.1029/2010GL045820, 2011. 6187

Oppenheimer, C., Francis, P., and Stix, J.: Depletion rates of sulfur dioxide in tropospheric volcanic plumes, Geophys. Res. Lett., 25, 2671–2674, 1998. 6185

Platt, U. and Stutz, J.: Differential Optical Absorption Spectroscopy – Principles and Applications, Physics of Earth and Space Environments, First Edition, Springer, Berlin, Heidelberg, New York, 597 pp., 2008. 6185, 6203

Real-time Environmental Applications and Display sYstem: Air Resources Laboratory, NOAA, available at: http://ready.arl.noaa.gov/READYcmet.php, last access: May 2012. 6212

Spinetti, C. and Buongiorno, M. F.: Volcanic aerosol optical characteristics of Mt. Etna tropospheric plume retrieved by means of airborne multispectral images, J. Atmos. Sol.-Terr. Phy., 69, 981–994, 2007. 6199, 6200

Title Page

Abstract | Introduction

Conclusions | References

Tables | Figures

|◄ | ►|

◄ | ►

Back | Close

Full Screen / Esc

Printer-friendly Version

Interactive Discussion

Stoiber, R. E., Malinconico, L. L., and Williams, S. N.: Use of the correlation spectrometer at volcanoes, in: Forecasting volcanic events, edited by: Tazieff, H. and Sabroux, J. C., Elsevier, Amsterdam, 424–444, 1983. 6185

Vandaele, A. C., Hermans, C., and Fally, S.: Fourier transform measurements of SO2 absorption cross sections: II. Temperature dependence in the $29\,000$–$44\,000\,cm^{-1}$ (227–345 nm) region, J. Quant. Spectrosc. Ra., 110, 2115–2126, 2009. 6195, 6203, 6217

Vogel, L., Galle, B., Kern, C., Delgado Granados, H., Conde, V., Norman, P., Arellano, S., Landgren, O., Lübcke, P., Alvarez Nieves, J. M., CÁrdenas Gonzáles, L., and Platt, U.: Early in-flight detection of SO_2 via Differential Optical Absorption Spectroscopy: a feasible aviation safety measure to prevent potential encounters with volcanic plumes, Atmos. Meas. Tech., 4, 1785–1804, doi:10.5194/amt-4-1785-2011, 2011. 6211, 6212

von Glasow, R., Bobrowski, N., and Kern, C.: The effects of volcanic eruptions on atmospheric chemistry, Chem. Geol., 263, 1–4, 131–142, doi:10.1016/j.chemgeo.2008.08.020, 2009. 6185

Table 1. Optical parameters and settings of the instruments used during the measurements.

IDOAS	
Co-added exposures per spectrum	10
Exposure time	0.5 s–2.5 s
Resolution (pixel $h \times v$)	175 × 255
Solid angle per pixel	0.26° × 0.05°
FOV per column	0.26° × 13.1°
Scanned solid angle	45.5° × 13.1°
SO$_2$-camera	
Exp. time Filter A	0.25 s–1 s
Exp. Time Filter B	0.1 s–0.3 s
Resolution (pixel $h \times v$)	1024 × 1024
Solid angle per pixel	0.02° × 0.02°
FOV	22.4° × 22.4°
NFOV-DOAS	
Co-added exposures per spectrum	15
Exposure Time	0.3 s–0.6 s
FOV	2.5°

Table 2. Average SO$_2$ emission rates for the measurement conducted at Popocatépetl. For all days, mean fluxes are shown for DOAS calibration and cell calibration and with or without correction of the radiation dilution effect.

	Day 1 1 March 17:01–18:02	Day 2 2 March[*] 15:35–16:10	Day 3 4 March[*] 15:16–17:30
Measurement Time [GMT]			
Wind direction [°]	283	313	119–125
Average Wind Speed [m s^{-1}]	10.2	9.4	8.0
Maximum SO$_2$ CD [molec cm^{-2}]	3.5×10^{18}	5.6×10^{18}	3.2×10^{18}
Distance [km]	6.8	6	8–8.5
DOAS calib. kg s^{-1}	10.56	14.34	4
Cell calib. kg s^{-1}	12.83	15.14	5
$\frac{\text{Flux Cell calib.}}{\text{Flux DOAS calib.}}$	1.21	1.06	1.25

[*] For 2 March and 4 March the fluxes are only a lower baseline for the flux.
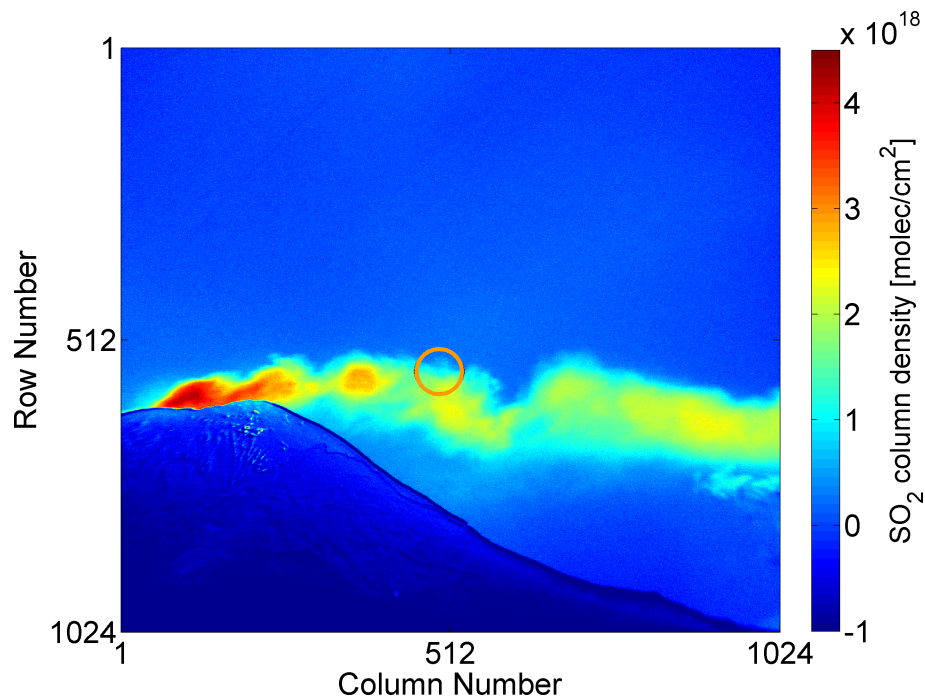
Fig. 1. SO$_2$ camera image from Popocatépetl acquired from Paso de Cortes on the 1 March 2011, the orange circle shows the field of view of the telescope of the NFOV-DOAS instrument used for calibration (see text).
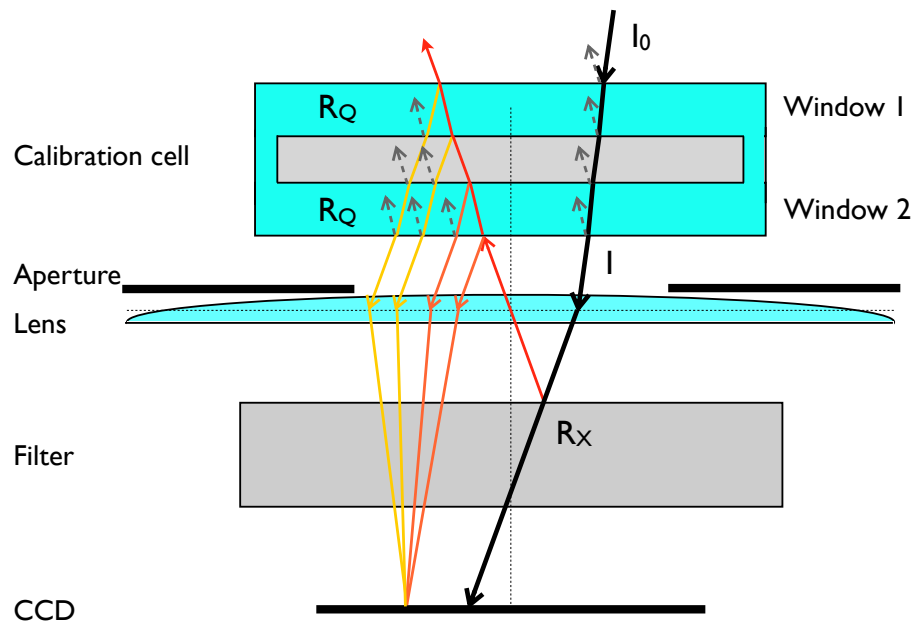
Fig. 2. Sketch of the optical set-up of the SO$_2$ camera (with a calibration cell in place). Reflections on the windows of the calibration cells, which are discussed in Sect. 4.4 are shown. Only part of the radiation arriving at the interference filter is transmitted (black line), radiation reflected from the interference filter (red) is – in turn – partially reflected on Window 1 (yellow) and Window 2 (orange) of the calibration cell. This radiation (some of which has passed the calibration cell three times) reaches the detector and leads to changes in the AA when arriving at the CCD. The grey dashed lines indicate additional reflections, that are only accounted for as losses in the calculation of the reflections. Note: reflections can also occur on the lens, but are neglected here since the reflectivity is greatly reduced by an anti-reflective coating.

Title Page

Abstract | Introduction

Conclusions | References

Tables | Figures

◄ | ►

◄ | ►

Back | Close

Full Screen / Esc

Printer-friendly Version

Interactive Discussion
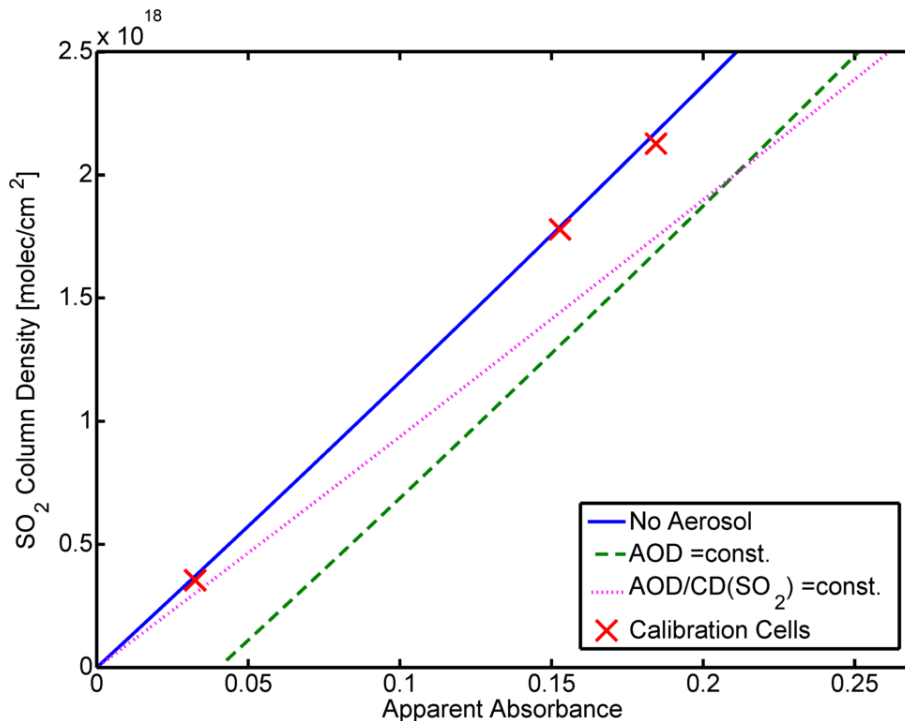
Fig. 3. Camera calibration curves simulated from a sky spectrum recorded with the DOAS spectrometer from Paso de Cortes, Mexico on 2 March 2011. The calibration curve for the no aerosol case (blue, slope of 1.185×10^{18} molec cm^{-2}) coincides with calibration cell measurements performed at the same time (red crosses). The curve for a constant AOD (shown for $\tau_{B,Aerosol} = 0.7$) (dashed green line) is parallel to the No Aerosol line, but is shifted by an optical density of 0.04. Assuming a linear relationship between the SO$_2$-CD and $\tau_{Aerosol}$, as we might expect in a real plume, we obtain the red dotted line. We here assumed $\tau_{B,Aerosol} = 1.0$ for an SO$_2$-CD of 2.0×10^{18} molec cm^{-2}. The slope is reduced when compared to the other cases (9.57×10^{18} molec cm^{-2}). Details on the simulated camera retrieval can be found in Appendix A.
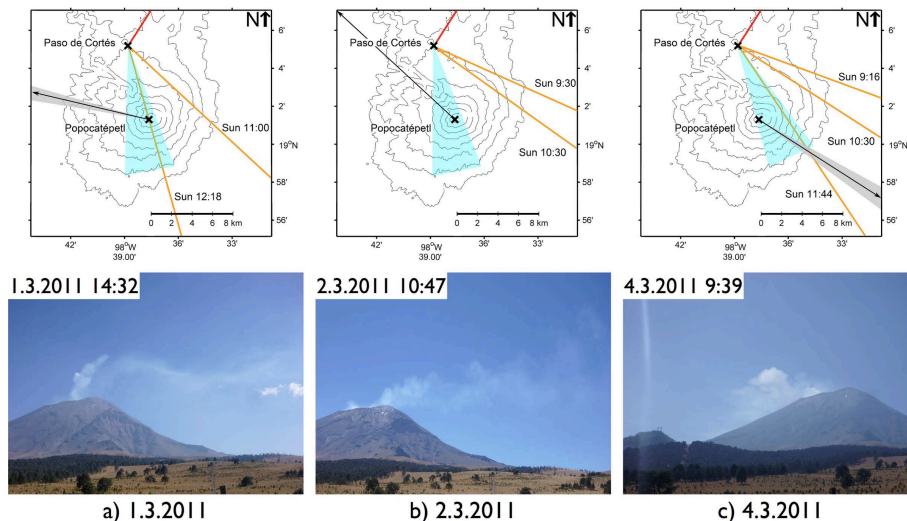
Fig. 4. Measurement geometry and photographs of the measurement conditions for the three days discussed in the text: **(a)** 1 March 2011, **(b)** 2 March 2011, **(c)** 4 March 2011. Top row: sketches of the measurement geometry. For all three measurement days the solar azimuth during the start and end time of the measurement is shown as orange lines. The camera field of view is depicted as a light blue area. The direction in which the calibration cell measurements were made is indicated by the red line. The black arrows show the general wind direction, the grey shaded areas indicate the range of wind directions. Bottom row: pictures of Popocatépetl and plume taken from the instrument position (Paso de Cortés) on all three days . The image from the 1 March 2011 was not taken simultaneously to the measurements, but the measurement conditions were similar.
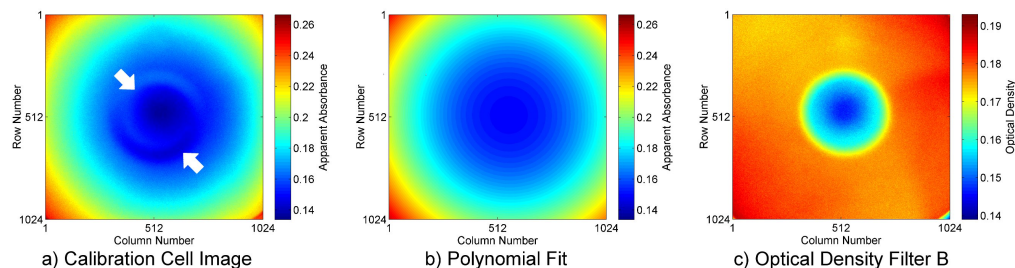
Fig. 5. (a) AA of a calibration cell with an SO$_2$ CD of 1.77×10^{18} molec cm^{-2}. A slight ring-like structure (arrows) is caused by reflections on the calibration cell. **(b)** AA image that was created from 2nd order polynomial fits to calibration-cell images. The area with reflections in the centre of the images was not considered when determining the best fits. These images were used as a mask to correct for higher sensitivity towards the edges in the IDOAS comparison and for the SO$_2$ fluxes. **(c)** Optical density τ_B for a calibration cell measurement with Filter B.
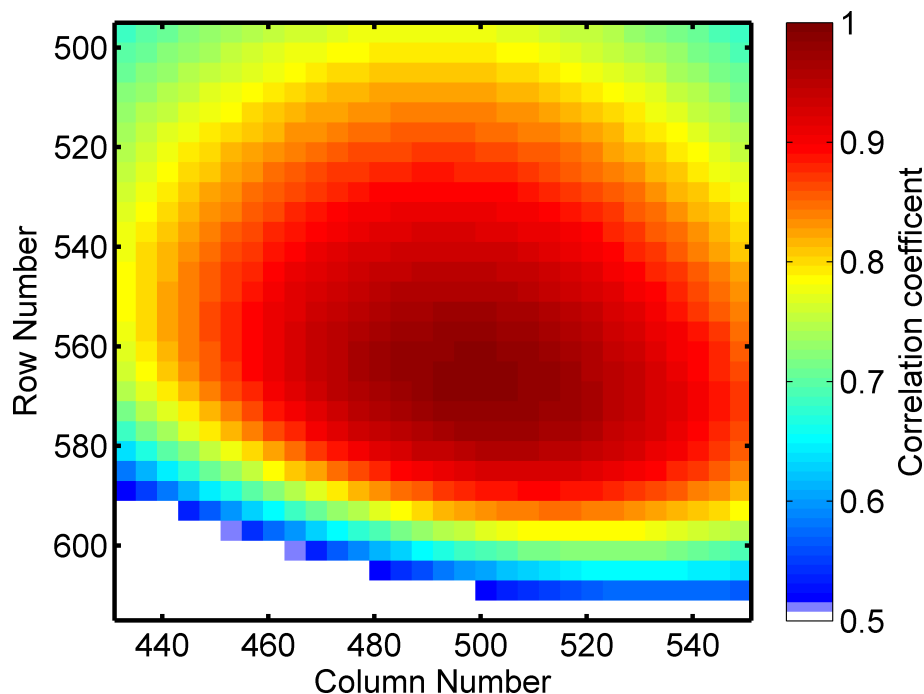
Fig. 6. The viewing direction of the NFOV-DOAS instrument was derived from the correlation coefficient between the SO_2 camera AA values and the NFOV-DOAS SO_2-CD's. The coordinates of highest correlation denote the position of the centre of the DOAS FOV in the camera image (Circle with a radius of 57 pixels). Correlation coefficients of 0.5 or below are shown white.

Title Page

Abstract | Introduction

Conclusions | References

Tables | Figures

|◄ | ►|

◄ | ►

Back | Close

Full Screen / Esc

Printer-friendly Version

Interactive Discussion
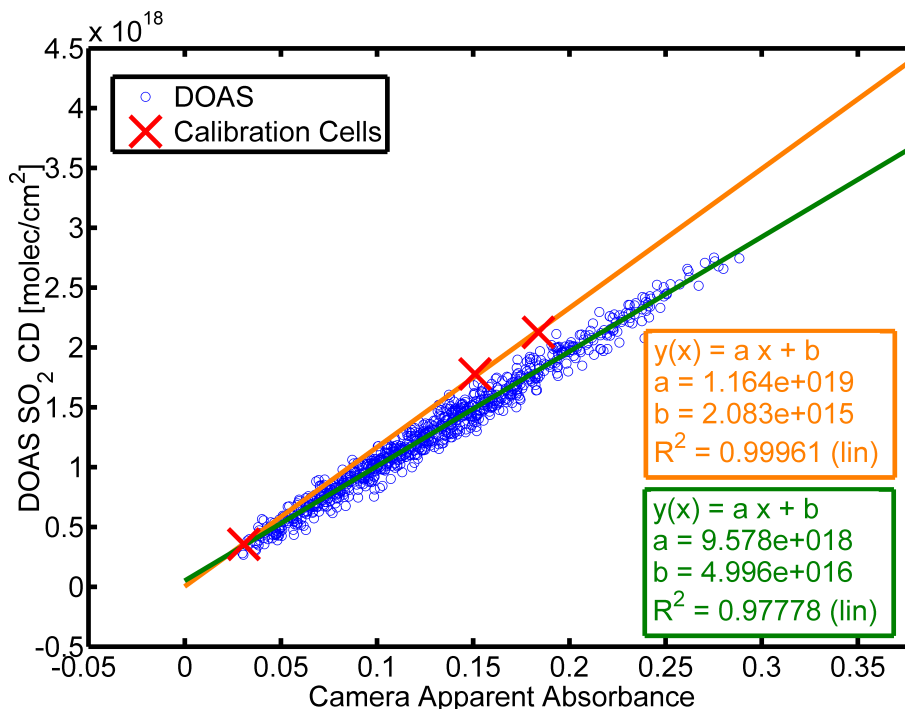
Fig. 7. Calibration curve for the SO_2 camera obtained from measurements performed on 1 March 2011 (Day 1). The SO_2 column density derived from the DOAS (blue circles) and calibration cells (red crosses) is shown as a function of the AA measured by the camera.

Title Page

Abstract | Introduction

Conclusions | References

Tables | Figures

|◄ | ►|

◄ | ►

Back | Close

Full Screen / Esc

Printer-friendly Version

Interactive Discussion
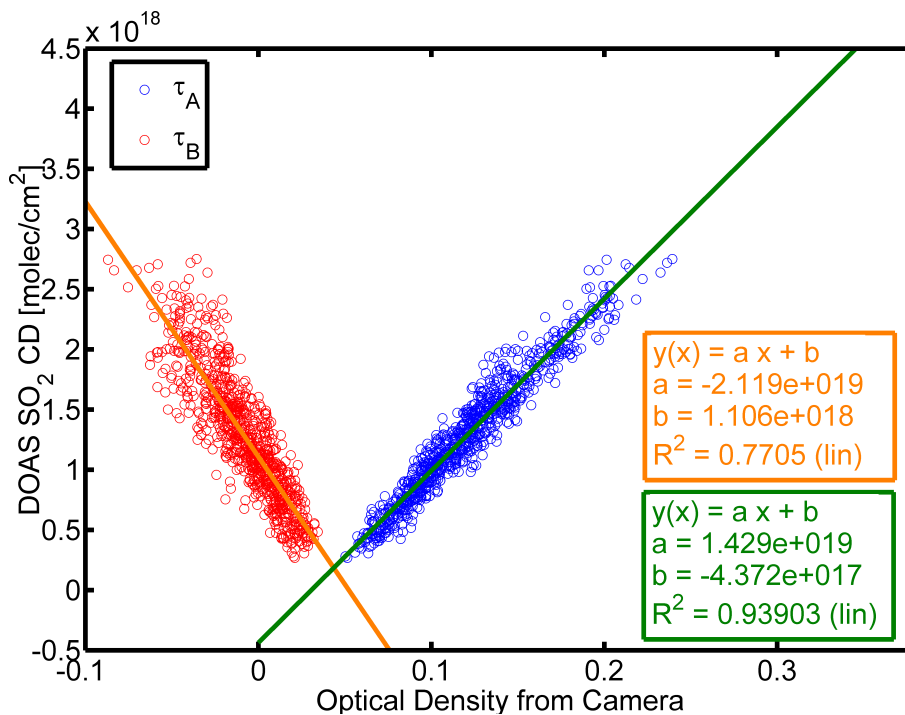
Fig. 8. The SO$_2$ column density from the DOAS plotted against τ_A and τ_B for measurements from 1 March 2011 (Day 1). Note the decreasing optical density τ_B for Filter B with increasing SO$_2$ column density caused by aerosol scattering in the plume.

Title Page

Abstract | Introduction

Conclusions | References

Tables | Figures

|◄ | ►|

◄ | ►

Back | Close

Full Screen / Esc

Printer-friendly Version

Interactive Discussion
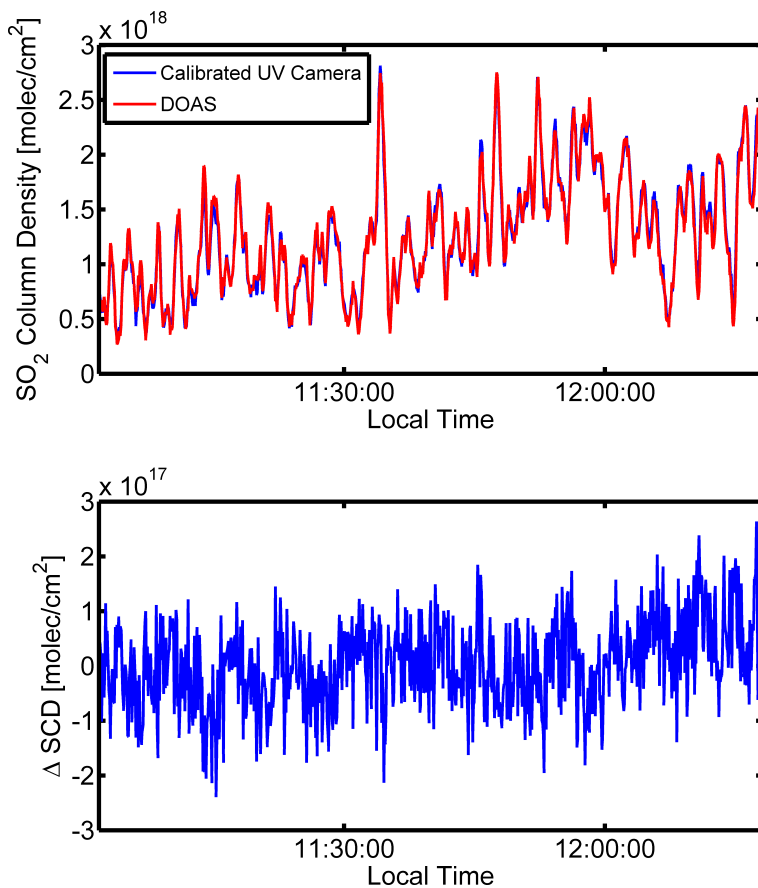
Fig. 9. Top: time series of the SO_2 camera (average values of all pixels coinciding with the DOAS) and the DOAS from 1 March 2011 (Day 1). SO_2 camera values were calibrated with the DOAS. Bottom: difference between the calibrated camera and the DOAS system.
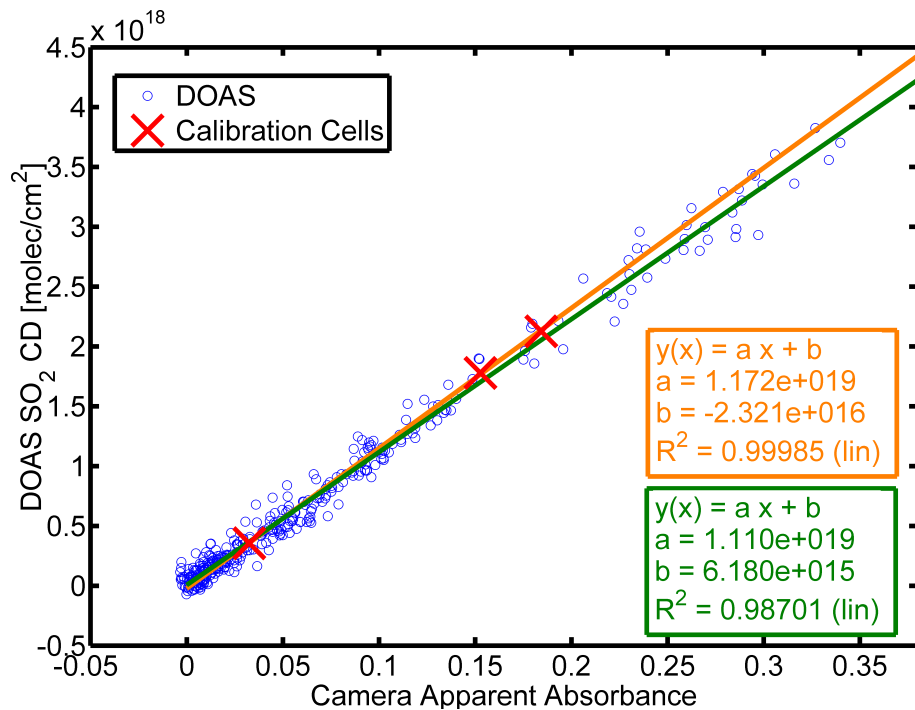
Fig. 10. Calibration curve for the SO_2 camera obtained from measurements performed on 2 March 2011 (Day 2).

Title Page

Abstract   Introduction

Conclusions   References

Tables   Figures

|◄   ►|

◄   ►

Back   Close

Full Screen / Esc

Printer-friendly Version

Interactive Discussion
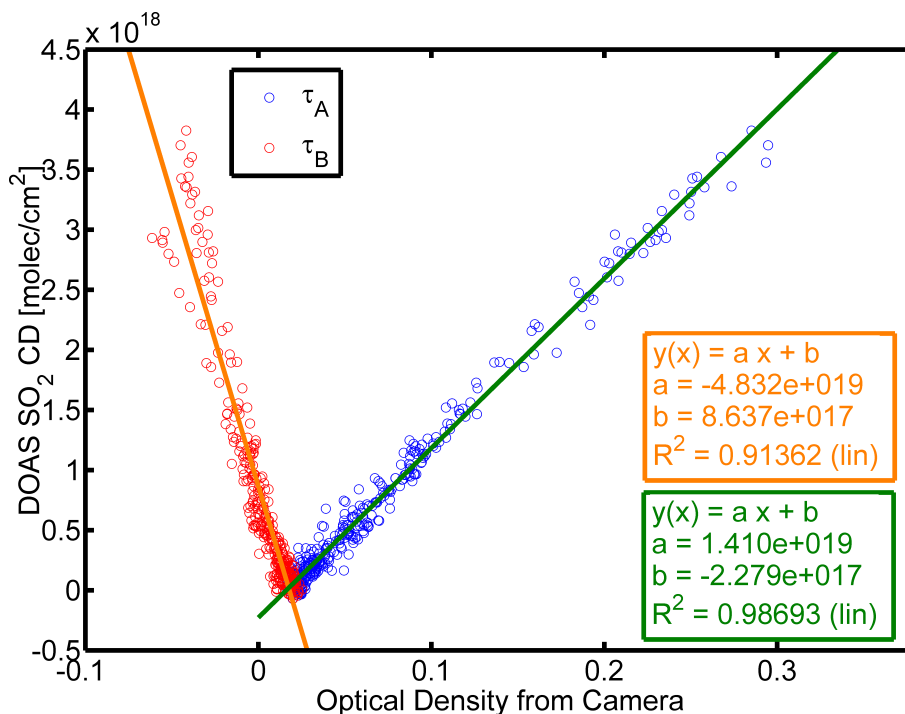
Fig. 11. SO_2 column densities from the DOAS plotted against the optical densities for Filter A and Filter B. Measurements from 2 March 2011 (Day 2) at Paso de Cortes.
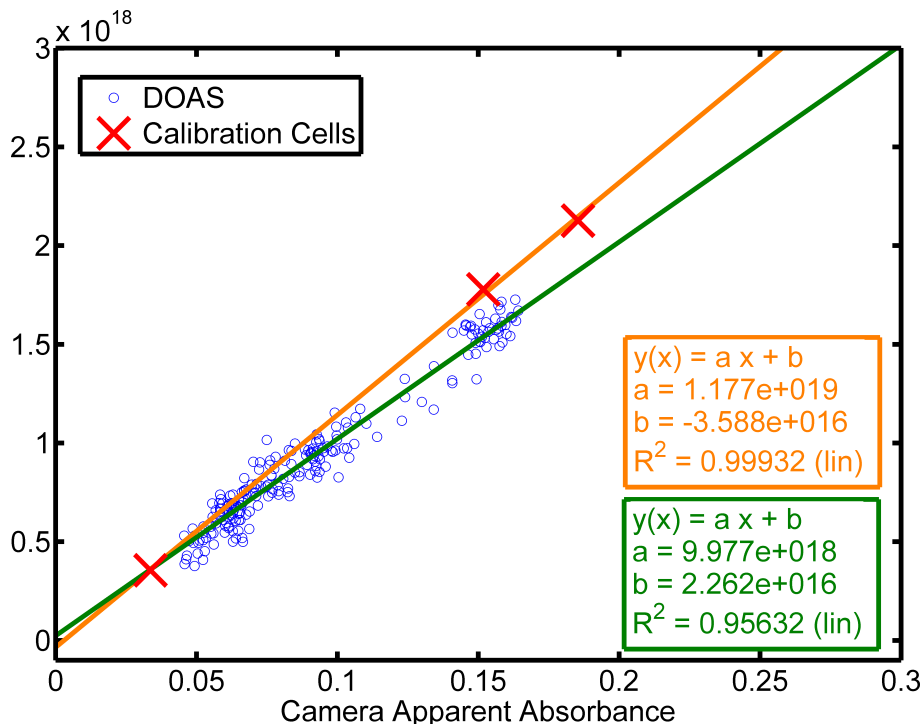
Fig. 12. Calibration curves for the SO$_2$ camera obtained from measurements performed between 09:15 a.m. and 09:36 a.m. on 4 March 2011 (Day 3).

Title Page

Abstract | Introduction

Conclusions | References

Tables | Figures

|◄ | ►|

◄ | ►

Back | Close

Full Screen / Esc

Printer-friendly Version

Interactive Discussion
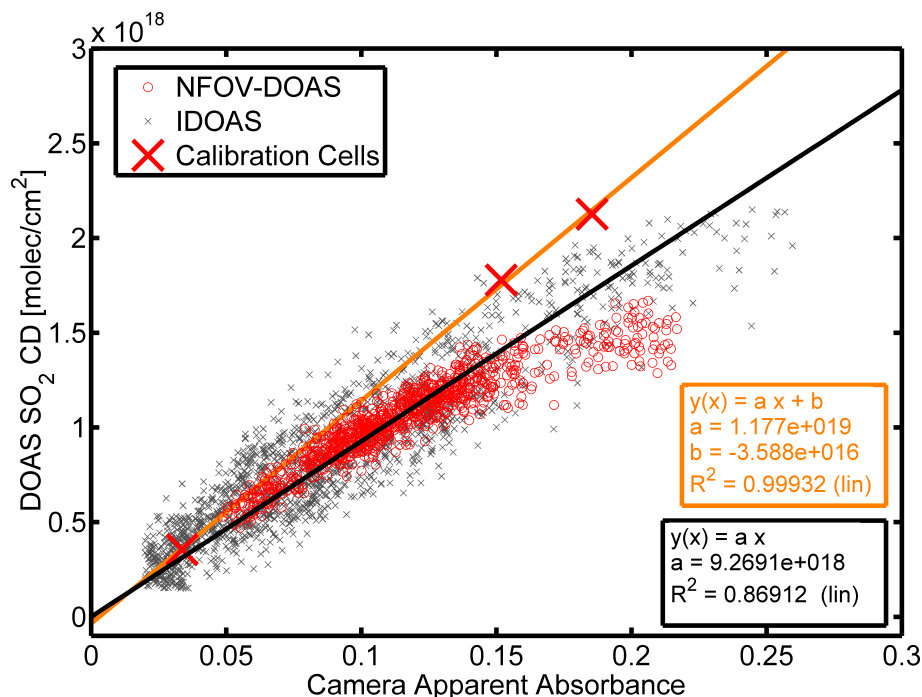
Fig. 13. Calibration lines from the NFOV-DOAS and from an IDOAS compared to the fit curve we obtained from the three calibration cells. For high AA values both DOAS instrument show a deviation from the calibration curve obtained from calibration cell measurements. The black curve is a linear fit to the IDOAS data that was forced through the origin. The data points from the NFOV-DOAS have higher AA values for high SO_2 CD's compared to this fit line.
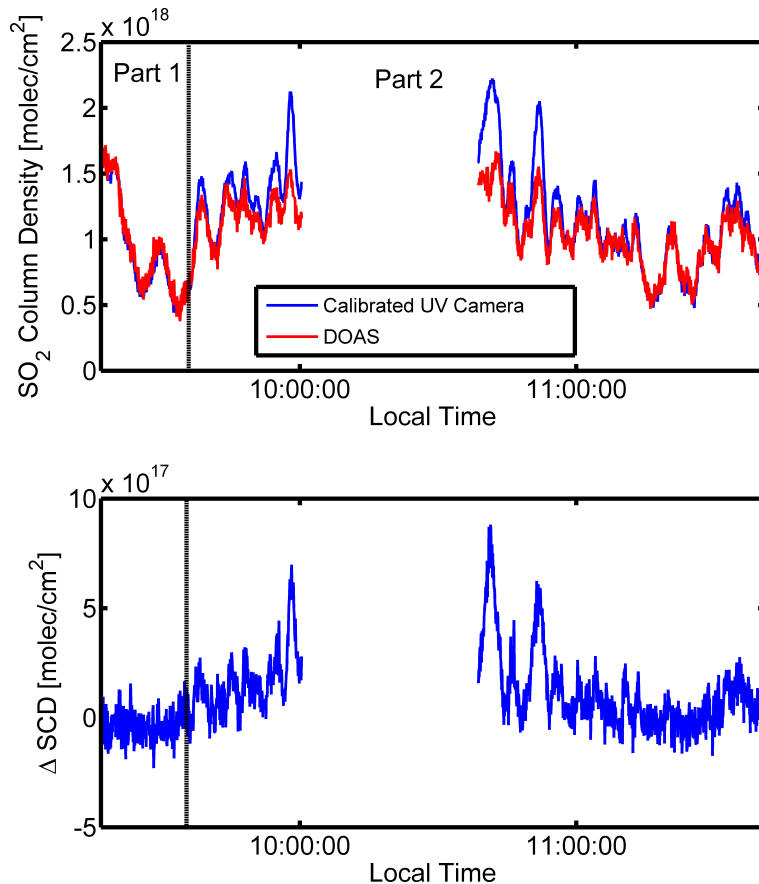
Fig. 14. Top: time series from the SO$_2$ camera on 4 March 2011 (calibration constant 9.98 × 10^{18} molec cm^{-2} obtained from Part 1) compared to the DOAS measurements. Bottom: difference between the camera and the DOAS system. Background images were acquired at 10:05 a.m. for the first time-series and at 10:36 a.m. for the second time series.

Printer-friendly Version

Interactive Discussion
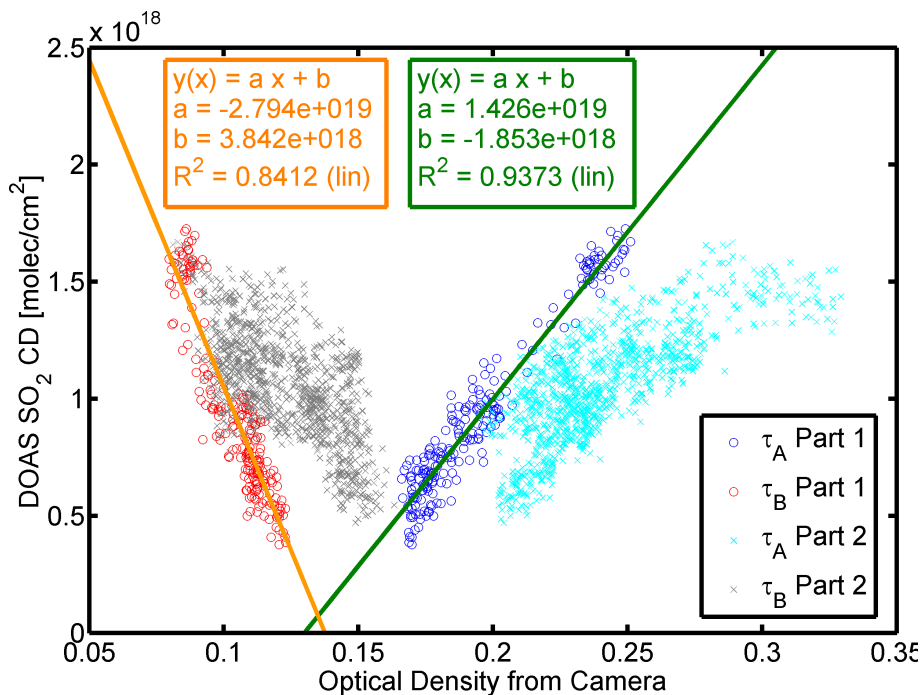
Fig. 15. SO$_2$ column densities from the DOAS measurements plotted against optical densities for Filter A and Filter B for the measurements on Day 3. We see that both optical densities are shifted towards higher values for Part 2.

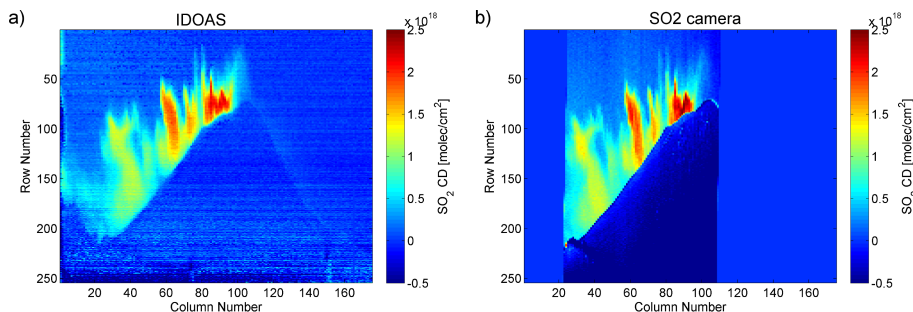Printer-friendly Version

Interactive Discussion

Fig. 16. (a) Image acquired with the IDOAS on the 4 March 2011 from Paso de Cortes. **(b)** Image constructed from the SO$_2$ camera measurements to match field of view and temporal resolution of the IDOAS measurements. For this image the camera images were calibrated with the black calibration line obtained from the IDOAS measurements depicted in Fig. 12.
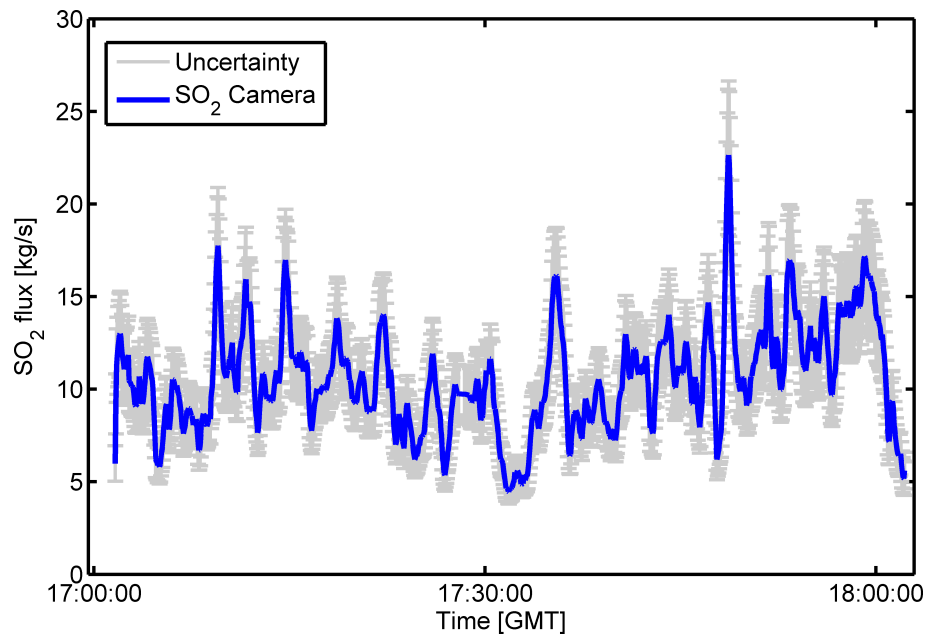
Fig. 17. SO$_2$ flux for 1 March 2011. The shown flux is radiation dilution corrected, the shown error consists of the wind-speed and the calibration error.